Chapter 2. Literature Review

2.1. Description of Solar Spectrum

The sun is a complex radiator with a spectrum that can be approximated by the spectrum of a 5525K (5250°C) black body. This spectrum is then modified and affected by many variation factors such as temperature across the sun's disk, Fraunhofer absorption lines, and the path length through the earth's atmosphere. It was reported that, up to about 70% of energy within the light arriving is absorbed by clouds, oceans and land masses. Figure 2.1 shows the solar radiation spectrum for direct light at both the top of the Earth's atmosphere and at sea level, as a function of wavelength, where the red part is the energy absorbed on sea level.
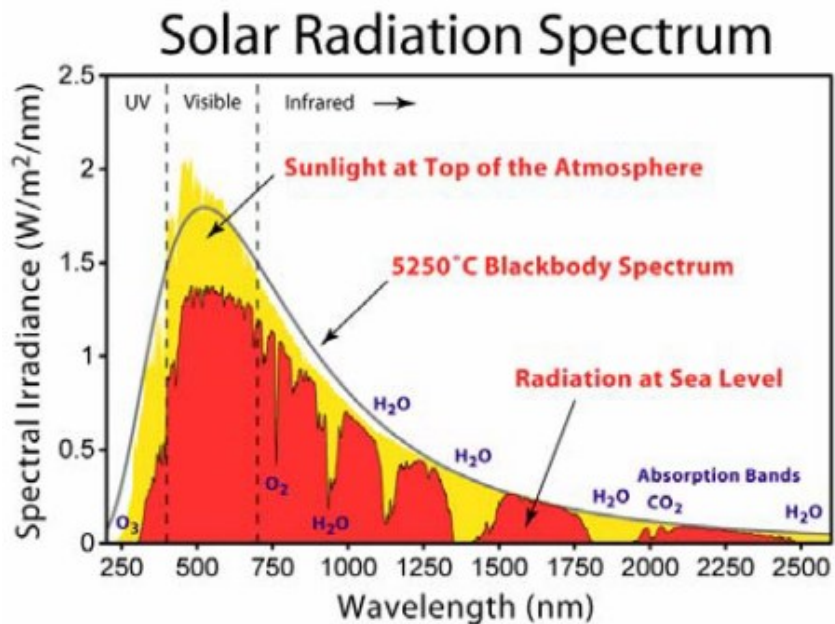
Figure 2.1. Solar radiation spectrum (Image created by Robert A. Rohde)[6]

When the sun is shining near its peak, with a relative modest 10% overall efficiency, 1kW of electricity would be generated for every 10m^2 of active area, which is equal to the average electricity per residence. However, as the sun doesn't shine at its peak intensity for whole day, electrical storage devices are required for all solar cell devices.

Based on quanta theory, the particle of light was called photon. Photon energy, E, is proportional to its frequency ν, and is given by the following Planck–Einstein equation:

$$E = h\nu = \frac{hc}{\lambda}$$
(2-1)

where h is Planck's constant (h= 6.626068×10^{-34} m²kg/s), and c is the speed of light (c=299,792,458 m/s). According to the wavelength, the light is including ultraviolet radiation (100 - 400 nm), visible light (400 - 700 nm) and infrared radiation (700 nm - 1 mm).

2.2. Titanium dioxide and its derivatives for alternative energy

2.2.1. Titanium Dioxide Nanoparticles

Titanium dioxide (TiO_2), which is also called as titania or titanium (IV), was first discovered in 1891, and was commercialized in 1961 as white pigment. Still then, it remains as one of the most promising and interesting materials due to its high photostability, high oxidation efficiency, non-toxicity, chemical inertness, biocompatibility, environmentally friendly nature, and low cost production. Since 1972, the phenomenon of photocatalytic splitting of water on TiO_2 electrode by Fujishima and Honda was firstly reported, then an exponential growth of research activities on TiO_2 and its derivatives have been seen in various applications, such as photovoltaics, photocatalysis, batteries, sensors, ultraviolet blockers, pigments, surface coating, and paints.[1–10]

TiO_2 belongs to the family of transition metal oxides. In nature, TiO_2 has four polymorphs: rutile (tetragonal), anatase (tetragonal), brookite (orthorhombic) and TiO_2 (B) (monoclinic).[11] In addition, four more structures were synthesized under high pressure, which are TiO_2 (II) with a PbO_2 structure, TiO_2 (H) with a hollandite structure, baddelleyite and cotunnite.[12–15] Among them, the two polymorphs anatase and rutile are mostly manufactured in chemical industry as crystalline materials. In fundamental studies, the anatase and rutile TiO_2 structures both have tetragonal structure but the distortion of interconnected TiO_6 octahedron is slightly larger for anatase phase.[16] In addition, each

octahedron of TiO$_2$ anatase is connected to 10 surrounding octahedrons, while those of TiO$_2$ rutile are connected to 8 surrounding octahedrons.[2] These differences in lattice structures are responsible for the mass densities and different electronic band gap energy structures between these two forms of TiO$_2$. The band gap energy of TiO$_2$ anatase phase is reported to be 3.2 eV, while the band gap energy of TiO$_2$ rutile phase is 3.0 eV. This relatively wide band gap means that both TiO$_2$ forms could be stimulated only under UV irradiation, and have low conversion efficiency under visible light.[17,18]
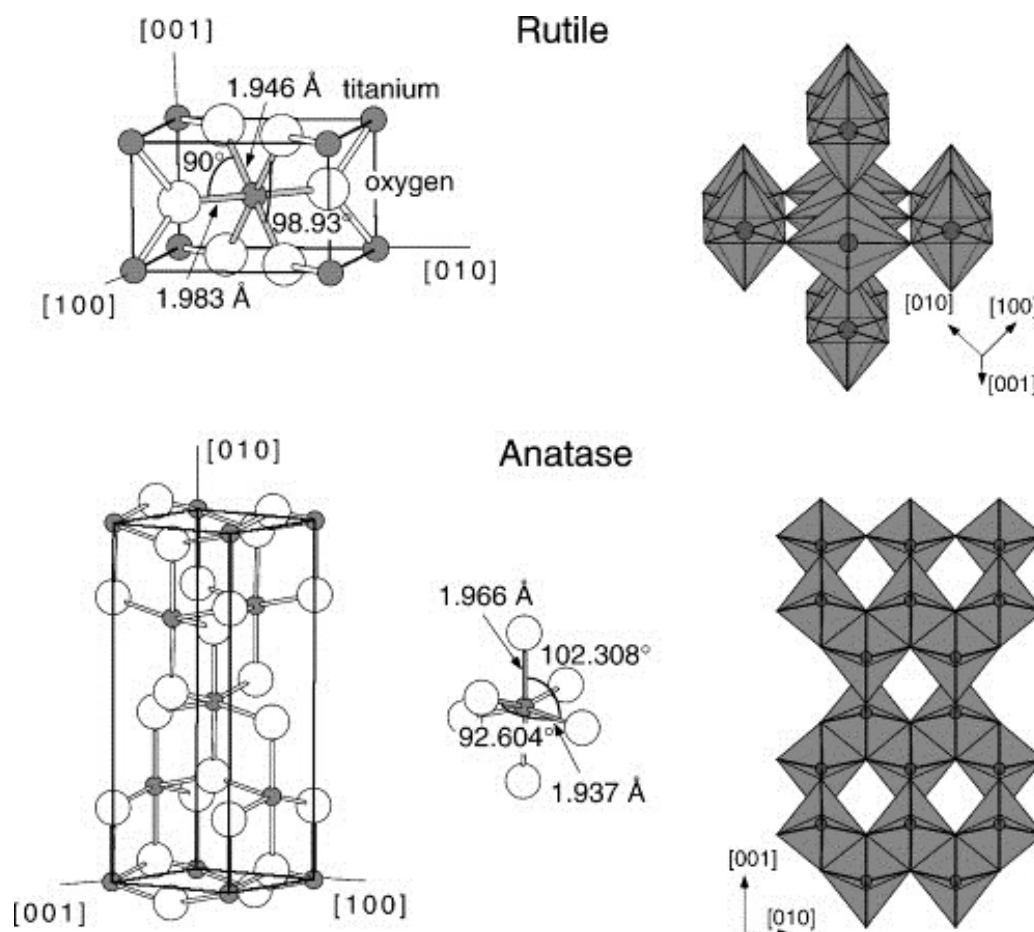
Figure 2.2. Crystal structures of TiO$_2$ rutile and TiO$_2$ anatase phase[19]

In general, the rutile is thermodynamically more stable than the anatase and brookite. Both anatase and brookite phases are converted to rutile phase at high temperature, around 750-800°C.[20] TiO$_2$ rutile phase is the mostly used form in the pigments industry. However, the activity of TiO$_2$ rutile phase as a photocatalyst under UV illumination is generally very poor. Recently, according to Sclafani et al., these activities

could be improved by changing its preparation conditions.[21] Differently, the TiO_2 anatase phase is metastable at low temperature, and it was reported to be preferred over other polymorphs for photocatalyst as well as for photovoltaic applications because of its higher surface area, higher electron mobility, lower dielectric constant and lower density.[22,23]

2.2.2. Coupled Colloidal Structures

Since TiO_2 NPs can only be excited by high energy UV irradiation with a wavelength shorter than 387 nm due to its relatively high energy band gap (3.2 eV), many investigations confirmed that the coupled colloidal structures, in which TiO_2 NPs is coupled with different semiconductor particles, would extend the light absorption range of TiO_2 from UV to visible light. This leads to an increase in charge separation, hence they result in higher activities in both photovoltaic and photocatalyst applications. Several coupled colloidal structures of TiO_2, such as CdS/TiO_2, ZnO/TiO_2, Fe_2O_3/TiO_2, SiO_2/TiO_2, SnO_2/TiO_2, Bi_2S_3/TiO_2, WO_3/TiO_2, and MoO_3/TiO_2 have been reported.[24–32] Among them, the coupled structure of CdS quantum dot and TiO_2 NPs has received the most attention.

CdS is a visible-light-driven photo-absorption with a narrow band gap of 2.4 eV. It has an absorption band between 450 - 470 nm for CdS nanoparticles, and at about 515 nm for the bulk crystalline CdS. Hence, CdS becomes an attractive candidate for photo-absorption under solar light. However, CdS is subjected to photoanodic corrosion in aqueous environment and has low quantum efficiency.[33,34] To overcome this stability problem and improve the photovoltaic and photocatalytic activity, CdS has been combined with a wide band gap semiconductor, such as ZnO or TiO_2, and this coupling gives reduced photogenerated electron-hole recombination.

2.3. H_2 Production via Photocatalysis Water Splitting

To replace or reduce the use of fossil fuels, another alternative ideal candidate for the energy generation is hydrogen which has to be produced from water using natural energies, such as sunlight. Hydrogen is the most abundant element and it exists in both

12

water and biomass. Its energy yield is high and is reported to be up to 122 kJ/g, which is largely higher than that of other fuels, such as gasoline (40 kJ/g).

Hydrogen obtained via solar water splitting is generally categorized in four different groups, which includes (i) water biophotolysis, (ii) organic biophotolysis, (iii) thermochemical water splitting and (iv) photocatalytic water splitting. Thermochemical water splitting system typically works at around 2000°C with the presence of a catalyst, such as ZnO[35], in order to perform water-splitting reaction, hence in large-scale production, this technique is often costly. In water biophotolysis, hydrogen is generated from water in the presence of light by cyanobacteria or green algae and special enzyme, such as hydrogenase or nitrogenase. This technology presents some difficulties in designing and scaling up the bioreactor for the process, and also in increasing the hydrogen yield production. Different from water biophotolysis, organic biophotolysis generates hydrogen by photosynthetic anoxygenic bacteria under light irradiation and anaerobic condition. Although organic biophotolysis gives a high hydrogen yield, this reaction will generate CO_2 as the by-product, hence it makes this technology less environmentally friendly compared to other technologies.

Compared to those three above technologies, hydrogen generated from photocatalytic water splitting has many advantages, such as production efficiency. Moreover, H_2 production from solar water splitting is environmentally friendly and has a great potential for low-cost and clean hydrogen production. In addition, H_2 can be easily distributed over large distances through pipelines or via tankers. It can also be stored in gaseous, liquid or metal hydride forms, and thus providing a huge market potential.

2.3.1. Working Principle

Photocatalytic water splitting to generate H_2 using solar energy is defined as the chemical reaction induced by photo-irradiation in the presence of semiconductor photocatalysts, where the electronic structure of semiconductor plays an important role in the reaction. When the semiconductors are excited by photons with energy higher than their band gap energy level, electrons are promoted from valance band (VB) to conduction band (CB). Separated electrons and holes migrate to the surface of the semiconductors and can respectively reduce/oxidize the reactants adsorbed by semiconductors.
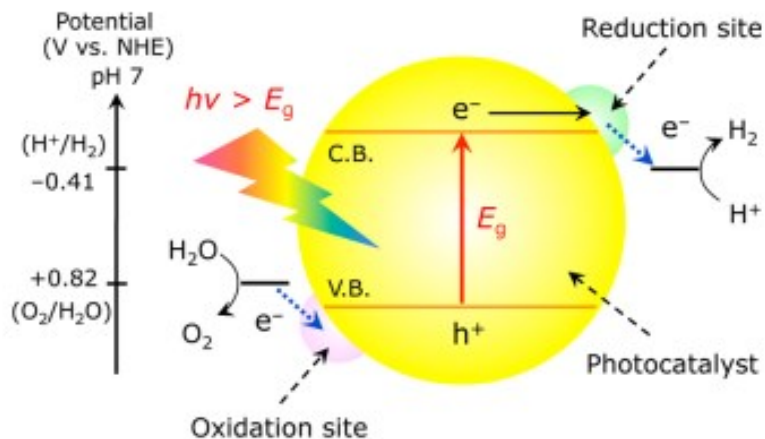
Figure 2.3. Principle of water splitting using semiconductor photocatalysts

Under the irradiation of light with energy greater than the bandgap of a semiconductor photocatalyst, electrons in the VB are excited and jump into the CB, resulting to the formation of an electron (e^-)/hole (h^+) pair. These photogenerated electrons and holes can participate in redox reactions on the surface of the photocatalyst, unless they recombine to give no net chemical reaction (Figure 2.3). To achieve overall water splitting, the top of the VB of a semiconductor photocatalyst must be more positive than the oxidation potential of H_2O to O_2 (0.82 V vs NHE at pH 7), and the bottom of the CB must be more negative than the reduction potential of H^+ to H_2 (−0.41 V vs NHE at pH 7). Therefore, the minimum photon energy thermodynamically required to drive the reaction is equal to 1.23 eV.

2.3.2. State-of-the-art of H₂ production based on TiO₂ NPs and its derivatives

In a photocatalytic water splitting reaction, the photocatalyst plays a crucial role. Most recently, extensive studies have been performed to split water under light irradiation, but the number of photocatalyst materials known is yet limited, and the activity efficiency is still low.[36,37]
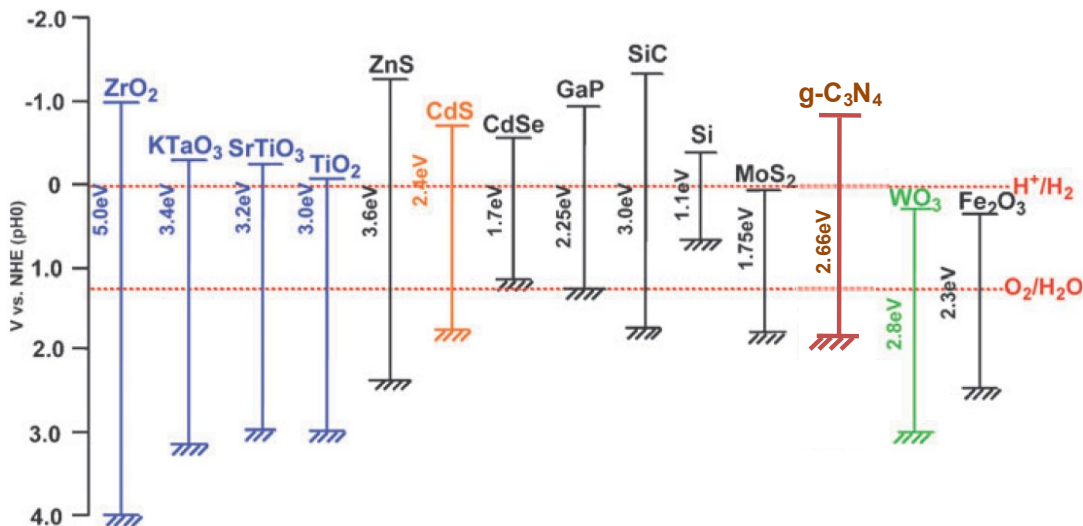
Figure 2.4. Relationship between the band structure of semiconductors and the redox potential of water splitting[38]

Metal oxides, such as TiO_2 and ZnO, have been extensively studied as photocatalysts for one-step water splitting, and some of them have achieved high quantum efficiencies as high as several tens of percent; however, these materials are inactive in the visible-light region. Beside, few metal chalcogenides, including CdS and CdSe, appear to be suitable photocatalysts for photocatalytic water splitting. They exhibit band gap energies sufficiently small to allow absorption of visible light and at the same time have conduction and valence bands at potentials appropriate for water reduction and oxidation. However, these chalcogenides are not stable in water, the S^{2-} and Se^{2-} anions are easier to oxidation than water, causing the CdS or CdSe catalyst itself to be oxidized and degraded before water.[39,40]

2.3.2.1. Modified-TiO₂ NPs-based Photocatalysts for H₂ Production Water Splitting

In general, TiO_2 has been widely used as photocatalyst for photocatalytic water splitting because it is stable, non-corrosive, environmentally friendly, abundant, and cost-effective. More importantly, its energy levels are appropriate to initiate the water-splitting reaction. However, pure TiO_2 NPs cannot easily split water into H_2 and O_2 in the simple aqueous suspension system due to the undesired electron-hole recombination reaction. In

addition, the wide band gap (3.0 eV for the rutile phase and 3.2 eV for the anatase phase) makes TiO_2 only active under UV region, which only covers less than 5% of the solar energy spectrum. So in order to utilize the visible light, which accounts for the major part of the solar spectrum (~45%), extensive investigations have been carried out to extend the photo-response of TiO_2 into the visible light region. It is also important to prevent the electron-hole recombination process during the photocatalytic water splitting. Effective approaches to achieve this goal have included noble metal loading, metal-ion implanting, non-metal doping, and organic dye sensitizing, and composite semiconductors. [41–53]

Several noble metals, including Pt, Au, Pd, Rh, Cu and Ag, have been reported to be very effective for enhancement of TiO_2 photocatalysis in H_2 production.[41–47] These selected noble metals normally have the Fermi levels lower than the CB of TiO_2, which would enhance the mobility of the photo-excited electrons transferred from the CB of TiO_2 to the metal particles.[50] Anpo et al.[47] found that the photocatalytic reactivity of semiconducting TiO_2 powder was dramatically enhanced by adding small amounts of Pt. By analyzing the Electron Spin Resonance (ESR) signals to investigate the electron transportation, the results indicated the occurrence of an effective electron transfer from TiO_2 to Pt particles. As the electrons accumulated on the noble metal particles then can be transferred to protons adsorbed on the surface and further reduce the protons to hydrogen molecules, thus this would be beneficial for water-splitting hydrogen production.[48,49] Bamwenda et al.[42] studied the hydrogen production activity from water-ethanol solution using Au and Pt loaded TiO_2 photocatalyst, which were prepared by deposition-precipitation, impregnation, photodeposition and colloidal mixing methods. The roles of Au and Pt on TiO_2 is to generate the attraction and trapping of photogenerated electrons, the reduction of protons and the formation and desorption of hydrogen. H_2 yield was observed to be dependent on the metal content on TiO_2 and showed a maximum in the ranges 0.3–1 wt.% Pt and 1–2 wt.% Au. However, the overall activity of Pt samples was generally about 30% higher than that of Au samples, which is probably a result of the more effective trapping and pooling of photogenerated electrons by Pt and/or because platinum sites have a higher capability for the reduction reaction. Sakthivel et al.[43] investigated the photo-oxidation of leather dye, acid green 16 in aqueous solution using Pt, Au and Pd deposited on TiO_2 NPs as photocatalyst. The photonic efficiency of Pt deposited on TiO_2 is almost comparable to the

16

efficiency of Au/TiO$_2$ but higher than that of Pd/TiO$_2$. In addition, the effect of metal contents on the photocatalytic activity was observed with metal deposition level of less than 1%. Increasing metal dopants resulted in a decrease of the surface area of TiO$_2$, the blockage of fine capillaries of parent TiO$_2$ surface, a reduction of photon absorption by TiO$_2$, and electron-hole recombination, leading to a lower water splitting efficiency. In additional, due to the high cost of Pt, Au, more research is needed to identify low-cost metals with enhanced photocatalytic activity, such as Cu and Ag. Sakata et al.[50] first showed that Cu-TiO$_2$ catalyst exhibit enhanced H$_2$ production from a water/methanol solution with photon energies within the visible-light region. Wu et al.[44] found that, by optimizing the loading of Cu, the hydrogen production activity was increased up to 10-fold times.

Another common practice for modifying the bandgap of the photocatalyst is the so-called metal ion doping practice, in which a small percentage of metal ions are incorporated into the crystal lattice of the photocatalyst.[51–55] Transitional metal ion doping and rare-earth metal ion doping have been extensively investigated for enhancing photocatalytic activities under visible light. Ikeda et al.[52] synthesized transition-metal (V, Cr, Fe, Co, Mo, or W) doped TiO$_2$ which displayed a higher visible light absorption intensity and a higher water splitting activity than pure TiO$_2$ under visible light irradiation. Peng et al.[53] carried out a systematic study the effect of Be metal ions doped TiO$_2$ on photocatalytic hydrogen production in the presence of ethanol as electron donors. It was found that the doping of metal ions could expand the photo-response of TiO$_2$ into visible spectrum, and could enhance the hydrogen production up to 75% compared to undoped-TiO$_2$. However, in case of deep doping, metal ions likely behave as recombination centers, which is unfavorable for the photocatalytic reactions. Therefore, metal ions should be doped near the surface of TiO$_2$ particles for a better charge transfer. Dholam et al.[51] synthesized Cr- or Fe-ion-doped TiO$_2$ thin films by radio-frequency magnetron sputtering and a sol–gel method to study hydrogen generation by photocatalytic water-splitting under visible light irradiation. H$_2$ production rates were recorded higher with Fe-doped TiO$_2$ (15.5 μmol·h^{-1}) than with Cr-doped TiO$_2$ (5.3 μmol·h^{-1}) because Fe ions trap both electrons and holes thus avoiding recombination. On the other hand, Cr can only trap one type of charge carrier. Other low-cost metals, such as Ni and Co,[54,55] were also found to be effective for photocatalytic activity enhancement.

These low-cost but effective metals are expected to be promising materials to improve photocatalytic activities of TiO_2 for practical applications. In recent years, many researchers have focused on TiO_2 with the double element co-doped TiO_2, which shows apparently higher photocatalytic activity than that of a single doped TiO_2. Ryo et al. [56] synthesized (Ni, Ta or Ni, Nb) co-doped TiO_2 photocatalysts, which displayed a higher visible light absorption intensity and a higher water splitting activity than pure TiO_2 under visible light irradiation. Recently, Sun et al.[54] prepared a single anatase phase of the Fe–Ni co-doped TiO_2 photocatalysts by alcohol-thermal method. The photocatalytic activities on H_2 evolution from water with ethanol as the sacrificial agent are studied in detail (Figure 2.5). The 5.0% Fe–4.0% Ni/TiO_2 particles displayed a good absorption of the visible light, and showed the average H_2 evolution rate is 361.64 $\mu mol \cdot h^{-1} \cdot g^{-1}$, which is higher than pure and single doped TiO_2 as a result of the large amount of H^+ and low recombination rate of electron–hole pairs in the reaction systems. The mechanism of H_2 evolution by water splitting over Fe–Ni/TiO_2 under visible light irradiation was proposed and showed on Figure 2.5d
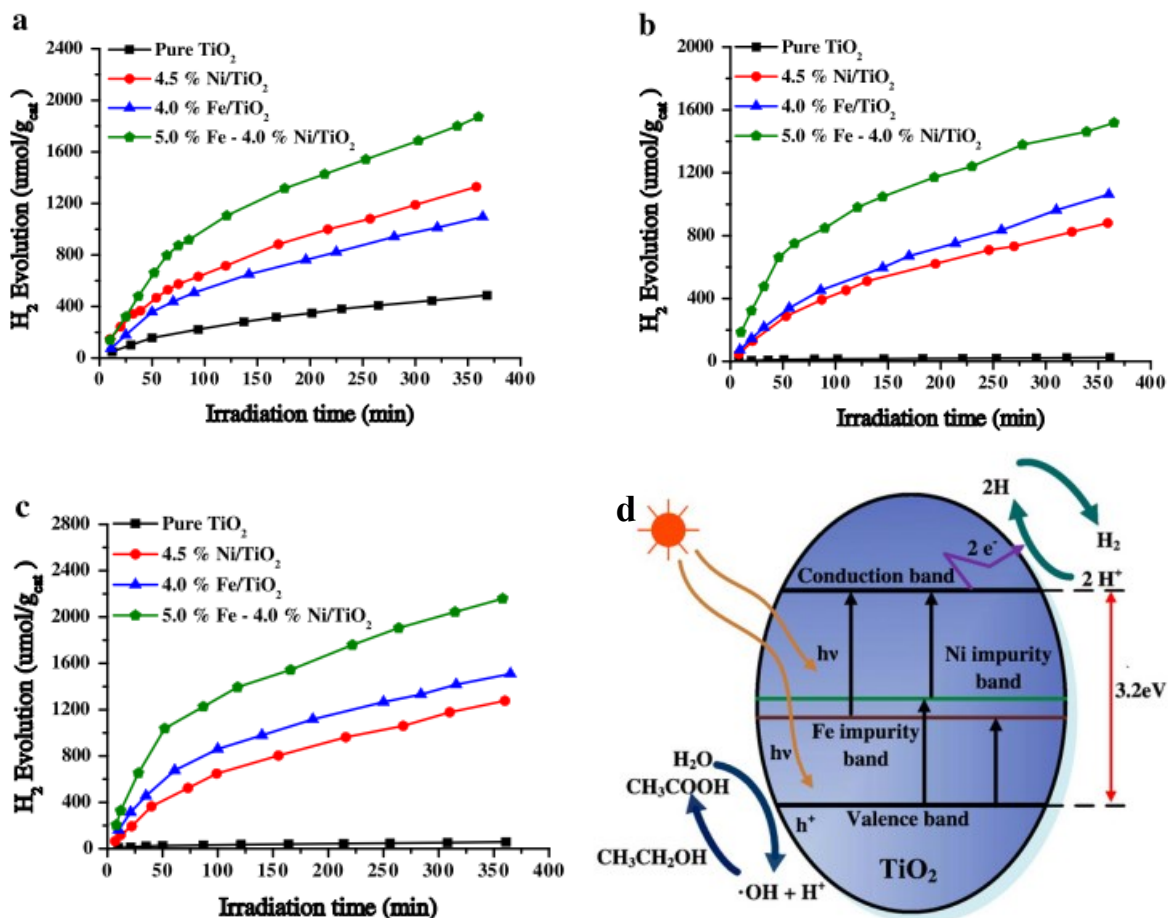
Figure 2.5. H₂ evolution by water splitting over TiO₂ catalysts (a) without any sacrificial agents and UV light irradiation; (b) without any sacrificial agents and visible light irradiation; (c) using ethanol as sacrificial agent and visible light irradiation; (d) Mechanism of H₂ evolution by water splitting over a Fe–Ni/TiO₂ photocatalyst under visible light irradiation

Beside the use of metal doping, anion doping is also used to improve the photocatalytic activity under visible light. It was reported that the doping of anions (N, F, C, S etc.) in crystalline TiO_2 could shift its photo-response into visible-light spectrum. Different from metal ions doped TiO_2, anion doped TiO_2 are less likely to form recombination centers; hence they are more effective at improving the hydrogen production activity. However, the ionic radius of S was reported to be too large to be incorporated into the lattice of TiO_2, and dopants P were found to be less effective as the introduced states were so deep that photo-generated charge carriers were difficult to be transferred to the

19

surface of the catalyst. Therefore, S- and P-doped TiO_2 were being less attractive as photocatalyst for the hydrogen production compared to N-/C-doped TiO_2.[57] Wang et al.[58,59] recently investigated that N-doped TiO_2 film with a narrow band gap of 2.65 eV was fabricated by RF magnetron sputtering and was successful applied as photocatalyst in hydrogen production without the assistance of metal cathode, bias, or loading noble metal. The H_2 production rate of the N-doped TiO_2 film was reported to be about 601 $\mu mol \cdot h^{-1} \cdot g^{-1}$, far higher than that of the undoped TiO_2 film and even about 50 times higher than that of dispersive TiO_2 P25 powder. Krengvirat et al.[60] studied the incorporation of C with TiO_2 and found that C-incorporated TiO_2 photoelectrodes with nanotubular structures provided higher photo-conversion efficiency (η) and hydrogen (H_2) evolution capability than those with irregular structures. The photoelectrode with an aspect ratio of ~142.5 had the remarkable ability to generate H_2 at an evolution rate of up to ~508.3 $\mu L.min^{-1}.cm^{-2}$ and η of ~2.3%.

The combination of TiO_2 and organic dyes sensitizing is a widely technique used in photocatalyst systems. The benefits of adopting dye-sensitized photocatalyst systems include the inhibition of charge recombination by improving electron-hole separation, the increase of spectrum response range of photocatalyst, and a change in the selectivity or yield of a particular product. Some of the frequently used dyes include Thionine (TH+), Toluidine blue (Tb+), Methylene blue (MB), Phenosafranin (PSF), Rhodamin B (Rh. B), Acridine orange (AO), Methyl violet, etc. Dhanalakshmi et al.[61] carried out a study to understand the effect of using $[Ru(dcpy)_2(dpq)]^{2+}$ as a dye sensitizer on photocatalytic hydrogen production from water under visible light irradiation. It was found that hydrogen production rate was enhanced by adsorbing dye molecules to the TiO_2; moreover, the hydrogen production rate did not further increase when additional Pt or dye loading beyond the optimal values.

The use of composite semiconductors is another strategy to increase the photocatalytic activity by achieving efficient charge separation and by expanding the absorption spectrum of the photocatalyst at the same time. This strategy is based on the coupling of a wide band gap semiconductor (non-oxide photocatalyst) with a narrow band gap semiconductor having a more negative CB level. With the difference in energy gap between two CB, the electrons can be injected from the smaller band gap semiconductor to

the larger band gap semiconductor; in our case from the CB of smaller band gap semiconductor to the CB of TiO_2. This would allow the extent in the absorption capacity of the mixed photocatalyst. Successful coupling of TiO_2 with other smaller band gap semiconductors for photocatalytic water splitting hydrogen production under visible light irradiation can be achieved when (i) the smaller band gap semiconductor should be able to be excited by visible light; (ii) the CB of the smaller band gap semiconductor should be more negative than that of TiO_2; (iii) and finally, the electron injection should be fast and efficient. Currently, coupled samples such as TiO_2/CdS, Bi_2S_3/TiO_2, TiO_2/WO_3, TiO_2/SnO_2, TiO_2/MoO_3, and TiO_2/Fe_2O_3 have been reported.

Sasikala et al.[62] presented the TiO_2/SnO_2 mixed oxide in which SnO_2 is in a dispersed phase on TiO_2, which have been synthesized by a polyol-mediated route. Photocatalytic activity of these samples for hydrogen generation from water using methanol as sacrificial reagent was studied under sunlight type radiation. The results showed that mixed oxide enhanced the photocatalytic activity for hydrogen generation compared to bare TiO_2 and the activity decreases with increasing SnO_2 concentration in TiO_2.

Similarly, it has been reported that coupling CdS with TiO_2 could improve the visible light response of TiO_2.[63–66] In this system, the photogenerated electrons move from CdS to TiO_2, whereas photogenerated holes remain in CdS. This charge-carrier separation stops charge recombination, therefore improves the photocatalytic activity of TiO_2. Optical absorption spectra analysis showed that CdS/TiO_2 could absorb photons with wavelength up to 520 nm. Under visible light illumination (Xe lamp), CdS/TiO_2 composite semiconductors produced hydrogen at a higher rate than CdS and TiO_2 used separately.[63]
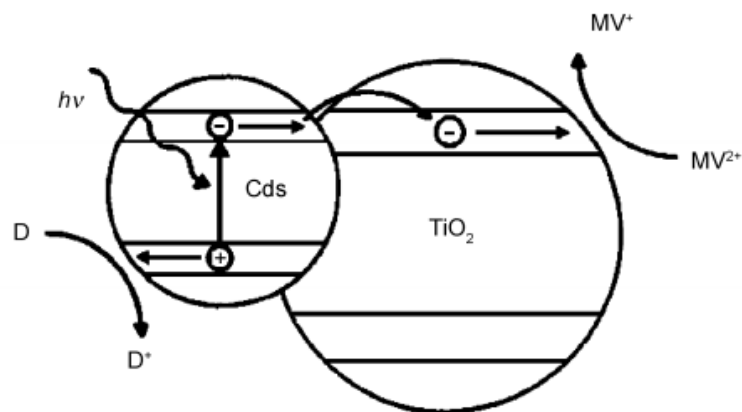
Figure 2.6. Schematic illustration of the photo-induced charge injection process that occurs upon excitation of the CdS component of a CdS/TiO₂ colloid in the presence of a sacrificial electron donor D.

Li et al.[64] conducted photocatalytic hydrogen production using CdS/TiO₂ composite semiconductors, which consist of CdS nanoparticles incorporated into TiO₂ nanotubes. The composite photocatalyst exhibited an unprecedented high rate of hydrogen production with an aqueous solution containing 0.35 M Na₂SO₃ and 0.25 M Na₂S as sacrificial reagents, and the apparent quantum yield for hydrogen production reached about 43.4% under visible light irradiation (Figure 2.7).
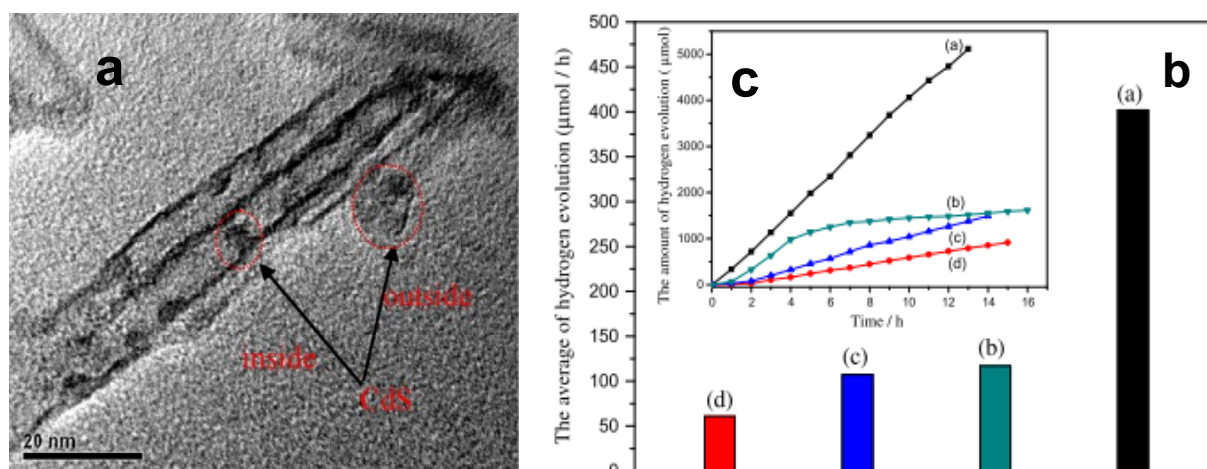
Figure 2.7. (a) TEM image of CdS/TiO₂ nanotube; (b) The average rate of H₂ evolution and (c) the amount of H₂ evolved vs irradiation time on various photocatalysts: (a) CdS/TiO₂ containing 13.44 wt% CdS ; (b) CdS/TiO₂ containing 8.32 wt% CdS; (c) the physical mixture of 20 wt% CdS/80 wt% TiO₂ nanotube; (d) a pure CdS powder.

22

Wu et al.[65] reported uniform and large-volume TiO_2 nanowires, which were successfully grown by a facile thermal treatment of titanium substrates assisted by KF in the presence of a H_2O vapor flow. The as-synthesized TiO_2 nanowires were further modified with hexagonal CdS QDs. The CdS/TiO_2 composite photocatalyst exhibited a very strong visible light response, and had the photocurrent density enhanced by over than 60% compared to the unmodified TiO_2 nanowires, which is promising for photocatalytic applications and hydrogen generation using the solar energy.

However, despite the improved activity of composite photocatalysts, most of the narrow bandgap non-oxide photocatalysts involved may encounter photo-corrosion problems in aqueous solution, which greatly confines their applications in hydrogen production photocatalytic water splitting. To overcome these photo-corrosion problems, a photocatalytic system called Z-scheme has been developed to generate H_2 and O_2 simultaneously. Basically, the Z-scheme consists of H_2 and O_2 photocatalysts to perform water reduction and oxidation, respectively (Figure 2.8).[67,68]
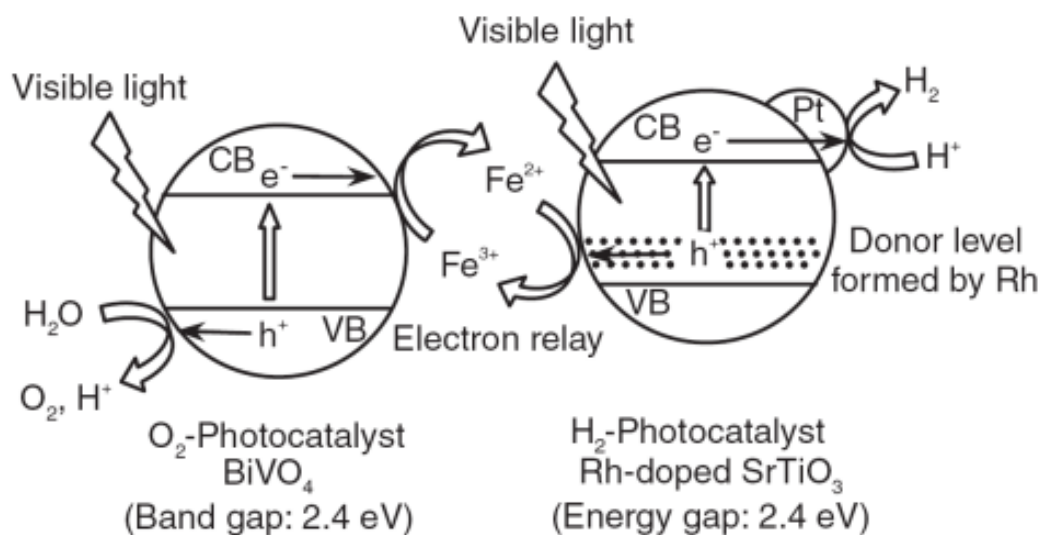
Figure 2.8. Mechanism of Z-scheme system for water-splitting.[68]

Since electron donors are consumed in the photocatalytic reaction, continuous addition of electron donors (sacrificial reagents or hole scavengers) is also required to sustain hydrogen production. It can also help to control the electron-hole recombination process.[69,70] Various compounds, such as lactic acid, methanol, ethanol, ethylene diamine tetra acetic acid derivative (EDTA), formaldehyde, Na_2S, Na_2SO_4, or ions, such as I^-, IO_3^-,

CN^-, and Fe_3^+ have been used as sacrificial reagents.[70–73] In their research, Nada et al.[71] carried out a qualitative investigation to study the effect of different electron donors on hydrogen production. It was found that the degree of hydrogen production was increased in the following order: lactic acid < ethanol < methanol < EDTA. Li et al.[74] added organic pollutants, such as formaldehyde, oxalic acid and formic acid, as electron donors into the photocatalytic reaction system. Decomposition of the organic pollutants was reported to be consistent with hydrogen production.

Besides their use as sacrificial reagents, the addition of carbonate salts was also found to improve the photocatalytic hydrogen production. Sayama et al.[50] found that the addition of carbonate salts to Pt-loaded TiO_2 suspensions led to highly efficient stoichiometric photocatalytic decomposition of liquid water into H_2 and O_2. These carbonate species, which covered the TiO_2 surface, can effectively suppress the back reaction of water splitting to form water and alleviate the photoabsorption of oxygen on the TiO_2.

2.4.   Photovoltaic Application

Solar cell or photovoltaic technology is one of many alternative renewable energies, such as wind, biomass and water. Solar cells present three unique properties: i) direct generation of electricity from solar radiation without the need of generators, ii) supplying electrical power in form of portable modules, and iii) it is the only energy that can be customized according to the need of uses. Thus, it is not surprising that since its first discovery, photovoltaic solar cells (PV) are becoming a great potential solution to the growing energy challenge and essential components of future global energy production. However, the big drawback of current PV technologies is their rather high production cost compared to other types of energies. They are about 10 times more expensive than energy from fossil fuel and about 3 times more expensive than other renewable energies.

The term 'photovoltaic' is derived from the combined Greek words for light, photos, and voltaic, named after Alessandro Volta. The development of photovoltaic cells began with the work of the French physicist, Antonie-Cesar Becquerel, in 1839.[75] Becquerel discovered the photovoltaic effect while experimenting with a solid electrode in

an electrolyte solution. He observed a small voltage and current when light fell upon the electrode. About 50 years later, in 1877, Charles Fritts constructed the very first solar cell device using a junction composed of semiconductor selenium layer and an ultra-thin, nearly transparent layer of gold.[76] However, the efficiency of the developed device transforming the absorbed light into electrical energy was less than 1%. By 1927, solar cells made of copper and the semiconductor copper oxide had been developed but still had energy conversion efficiency of less than 1%. In 1941, with the invention of silicon solar cells made by Russell Ohl, the energy conversion efficiency had been largely improved. In 1954, Pearson et al. [76] opened a new era of semiconductor photovoltaic material when he obtained a silicon solar efficiency of about 6%. In 1989, concentrator solar cells (types of cells where sunlight is concentrated onto the cell surface by means of lenses) achieved an efficiency of around 37% due to the increased intensity of the collected energy.

In the energy market, the competitive position of each solar technology is mainly determined by the three factors: efficiency, lifetime and cost. As an alternative and effective energy source, a solar cell must generate at least enough energy in its operating lifetime in order to payback the financial and energy cost required to produce the cell. It is estimated that an operating lifetime of a cell of about 20 years would be a workable value. The operating lifetime may be affected by many external factors, such as physical damage, corrosion, deterioration of cell support structures, etc. Also, it could be affected by internal material-related factors like materials degradation, diffusion, photogeneration of defects, etc. Especially, for those solar cells that are used in space, radiation damage is also a major factor in degrading cell performance.

Figure 2.9. Current state of solar cell efficiencies (Reprint from National Renewable Energy Laboratory (NREL) website)

Up-to now, solar cells have been classified into four generations based on the materials and the processing technologies used to fabricate the devices. The most recent generation is the fourth generation, which includes hybrid solar cells, where the electron acceptor and transporter are grown in self-organized structures on a substrate, filled with a conjugated polymer as hole transporter. In general, this type of solar cells is based on inorganic semiconductor nanoparticles and polymer materials; hence it combines the unique properties of inorganic semiconductor nanoparticles, high electron mobility, and organic materials flexibility and their easy solution processing. Recently, various hybrid bulk heterojunction solar cells have been reported. Highest efficiency for these devices had been obtained with CdSe nanoparticles and polythiophene.[77]

Despite the low energy conversion efficiency, the strongest argument for the newest generation solar cells is certainly their promising ultralow cost. The vision for solar cell materials is based on thin film plastic carriers, using materials like solution-processable organic and inorganic semiconductors, which are generally manufactured by coating and printing techniques that are highly attractive from an economic standing point. The new

26

generation of solar cells are also attracted by their unique features like the potential to be flexible and semitransparent and their potential to be manufactured in large area coating by continuous printing processes.

2.4.1. Working Principle

In hybrid organic/inorganic solid-state devices, as the polymer is illuminated by photons of energy higher than the band gap, electron-hole pairs are generated [78]. An electron is then promoted from the highest occupied molecular orbital (HOMO) to the lowest unoccupied molecular orbital (LUMO), forming an exciton. The formed excitons diffuse into the organic material and can reach the depletion layer where the internal electric field can induce the separation of the charge carriers. The photogenerated holes can thus migrate along the polymer, while the electrons can move along the nanocrystalline network, then collected via the respective electrical contacts (Figure 2.10).
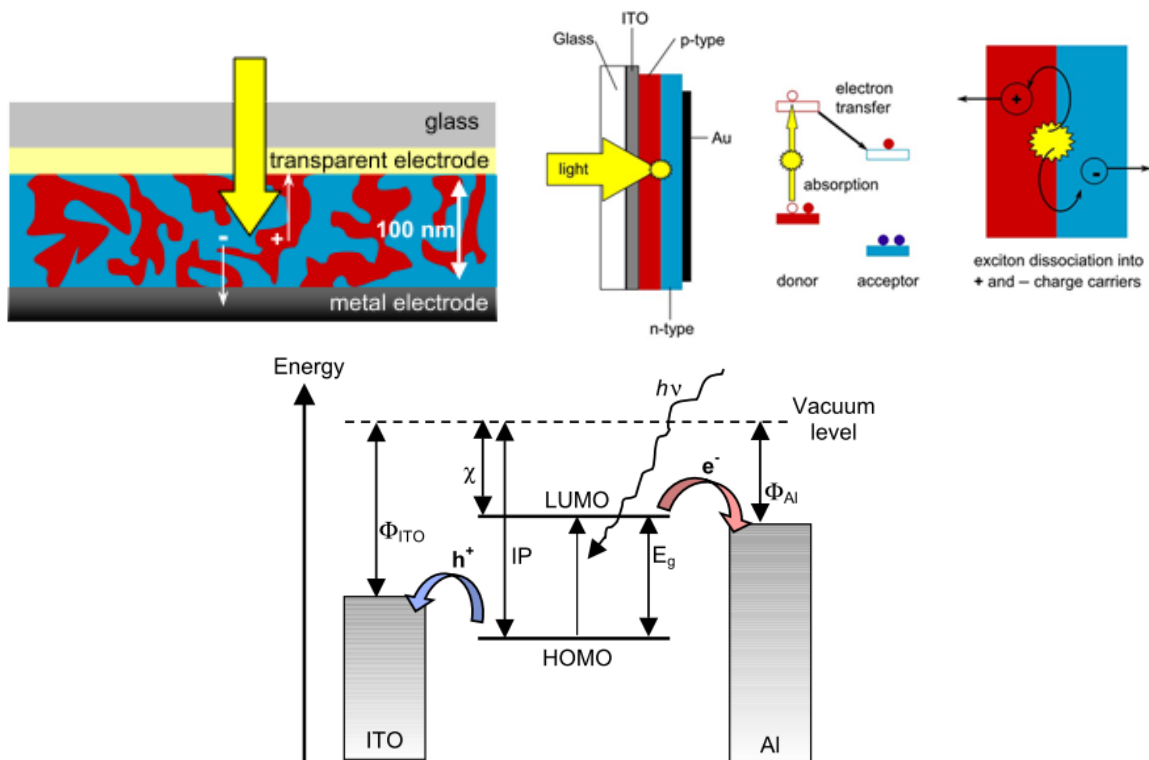
Figure 2.10. (a) Structure of BHJ solar cells (b,c) Scheme drawing of the working principle of an organic photovoltaic cell.

In general, for a successful hybrid bulk heterojunction solar cell, four important processes must be optimized to obtain a high conversion efficiency of solar energy into electrical energy, which include the absorption of light, charge transfer and separation of the opposite charges, charge transport and charge collection. In PVs, charge recombination of the photogenerated electron-hole pairs is the major disadvantage in the use of conjugated polymers as an active layer. In conjugated polymers, the diffusion length of excitons is typically about 5−15 nm, so the light excitation occurring far from the interfaces will decay without any charge transfer from the polymer to the nanocrystals.[79,80] Charge separation can be enhanced at the interface with a material of higher electron affinity, so that carriers can be easily transferred because of the favorable energetic states in the junction energetic diagram. Besides, a large interface between the two materials is also needed in order to achieve an efficient photoconductivity.

To overcome this limitation, blending between conjugated polymers and nanosize crystal oxides (especially particle sizes in the range of 2–10 nm) has been recently proposed.[81] This could create a large interface between the polymer matrix and the dispersed nanoparticles, leading to an enhancement of charge transfer inside the nanocomposite. This condition facilitates the diffusion of the photogenerated excitons to the interface, where the separated charge carriers may travel to the respective contacts, thus delivering current to the external circuit.[81]

2.4.2. Solar Cell Characteristic

2.4.2.1. Solar Irradiance Air Mass

The path length through the atmosphere is of fundamental importance. This path length can be conveniently described in terms of air mass, m_r. Basically, it is the ratio of the path length of the sun rays through the atmosphere when the sun is at a given angle θ to the zenith.
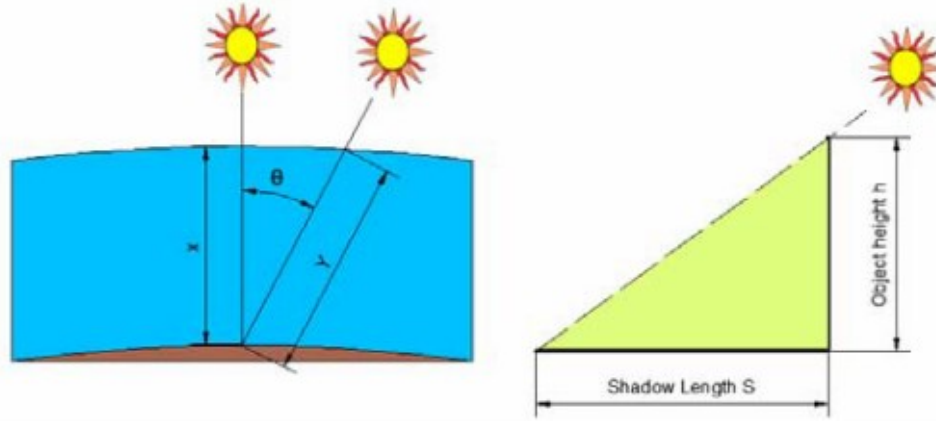
Figure 2.11. Air mass measurement

The equation that is provided to calculate the air mass is given by the following equation:

$$AM = \frac{1}{\cos\theta + 0.50572(96.07995 - \theta)^{-1.6364}} \qquad (2\text{-}2)$$

The reference solar spectral irradiance AM0 (Air Mass 0) represents the irradiance at the top of the atmosphere with a total energy of 1353W/m². In characterization, an air mass distribution of AM1.5 corresponds to the spectra power distribution observed when the sun's radiation is coming from an angle to over head of about 48.2º and the total energy equals 1000W/m².

An ideal and perfect solar cell that would be expected to cover the entire spectrum and to convert all this energy into electricity would have an efficiency of 100 %. However, in reality, depending on the semiconductor used, only a part of the solar spectrum is covered and utilized (Figure 2.1).

In addition to the direct irradiance, we also have to consider the diffused irradiance, which is predominant on a cloudy day, and also the reflected irradiance. Reflected irradiance is dependent on the albedo, which is a measure of the reflectivity of the Earth's surface. Fresh snow has an albedo of around 80 %, desert sand 40 % and grass between 5 and 30 %.

2.4.2.2. The short-circuit current (I_{SC}) and the Open-circuited voltage (V_{OC})

The current to voltage curve of a solar cell has a very characteristic shape and can be described by the mathematical models of an ideal or real photovoltaic generator.[82] When the p–n junction is illuminated by the sunshine, an electron–hole pair is generated by the photons that have energy greater than the energy bandgap. The number of electron–hole pairs is proportional to the light intensity. Because of the electric field in the depletion region due to the ionized impurity atoms, the drift of electrons toward the n-side and that of holes toward the p-side occur in the depletion region. This charge separation results in the current flow from n- to p-side when an external wire is short-circuited (Figure 2.12).
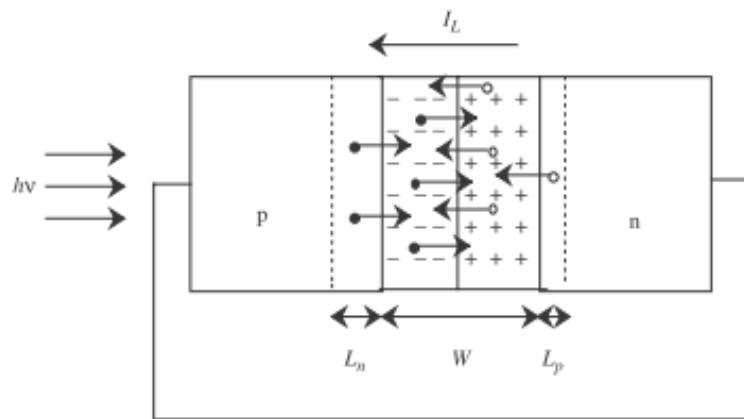
Figure 2.12. Schematic illustration of carriers flow in short-circuited external circuit.

When the p- and n-sides are short-circuited, the current is called short-circuit current I_{SC} and is equals to the photogenerated current I_L if the series resistance is zero. When the p- and the n-sides are isolated, electrons move toward the n-side and holes move toward the p-side, resulting in the generation of a current potential. The voltage developed is called the open-circuit voltage V_{OC}.
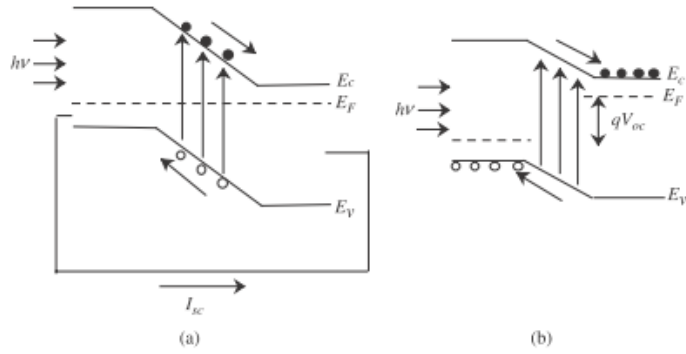
Figure 2.13. Illumination energy band diagrams of p–n junction in (a) the short-circuited and (b) open-circuited current.

Assuming that the area of the solar cell is unity, the current characteristic of the illuminated p–n junction is given by the following equation:

$$I = I_0(e^{qV/nkT} - 1) - I_{SC} \qquad \text{(2-3)}$$

where I_0 is the reverse saturation current (A).

In the open-circuit, which is obtained for $I = 0$, the voltage is given by equation:

$$V_{OC} = \frac{nkT}{q}\ln(\frac{I_{SC}}{I_0} + 1) \qquad \text{(2-4)}$$

When the solar cell is operated under a condition that gives the maximum output power, the voltage V_m and the current I_m at the optimal operation point are shown in the following Figure 2.14.
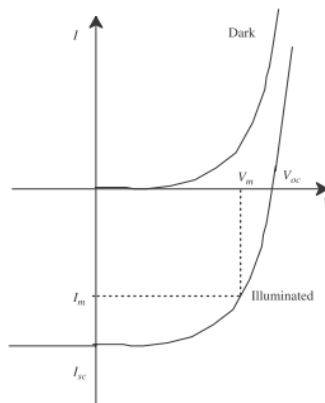
Figure 2.14. Current–voltage characteristics of p–n junction under illumination and darkness.

In between these two points where in both cases the retrieved power is zero, there is a working point, called the maximum power point, where the power that can be retrieved is the highest and equals to: $P_m = V_m I_m$. It is precisely at this point that the cells should be used and the ratio between P_{max} and the light intensity represents precisely the cell efficiency. However, the curve, and thus this point, are not fixed and vary depending on many parameters.

The relationship between the ratio of the maximum output power with the product of I_{SC} and V_{OC} is defined as the fill factor (FF).

$$FF = \frac{V_m I_m}{V_{OC} I_{SC}}$$

(2-5)

For a simple single-semiconductor photovoltaic model, the FF lies between 0.25 and 1.0.

2.4.2.3. Power conversion efficiency (PCE or η_e) and Quantum efficiency (QE)

The power conversion efficiency is the essential parameter for solar cell with respect to energy power and cost. The overall efficiency η_e of a solar cell is calculated by the following equation:

$$\eta_e = \frac{V_{OC} I_{SC} FF}{P_{in}}$$

(2-6)

where I_{SC} is the short circuit current density in A/m² (current for V=0) and P_{in} (W/m²) is the light incident solar radiation on the device as measured by a calibrated reference cell.

The last important parameter experimentally accessible is the variation of I_{SC} with the wavelength (λ) of the incident light. This value is called external quantum efficiency (EQE) or incident photon to collected electron (IPCE), which gives the ratio of the collected charge carriers per incident photons:

$$EQE = \frac{1240 \times I_{SC}}{\lambda \times P_{in}}$$

(2-7)

where λ is given in nanometer (nm), I_{SC} in amperes per meter squared (A/m^2), and P_{in} in watts per meter squared (W/m^2). As the short circuit current density (I_{SC}) does not necessarily increase linearly with the incident light power (P_{in}), the EQE values generally depend on the P_{in} of the monochromatic light. The value of EQE can be further corrected to take into account the different losses, like the reflection from the glass surface and the absorption by different nonphotoactive layers involved in the device. The IQE is related to the EQE by the reflectance (R) and the transmittance (T_{Tr}) of the solar cell by the following equation:

$$IQE = \frac{EQE}{(1 - R - T_{Tr})}$$

(2-8)

2.4.3. State-of-the-art of BHSCs based on TiO₂ NPs and their derivatives

In general, the bulk heterojunction ensures a higher interfacial area and thus an optimal donor-acceptor contact. Over the last decade, bulk heterojunction solar cells (BHJs) based on an interpenetrating network of electron donors and acceptors prepared using solutions of conjugated polymers have become attractive for use in inexpensive large area and low weight devices.[83–85] The reported power conversion efficiencies of polymer organic solar cells were about 4 to 5%; however, for practical applications, there are several factors that limit the efficiency, which include the poor stability of the active layer under the illumination, the poor overlap between the absorption spectrum of the polymer and the solar spectrum, phase segregation and the low mobility of charge carriers, especially electrons transportation.[86–89] One potential solution is the use of PVs based on inorganic semiconductor nanocrystals and conjugated polymers, due to the possibility of combining the superior conductivity of inorganic nanoparticles and optoelectronic properties of organic polymers. These systems are advantageous because they combine an inorganic material, which performs the task of electron transport, with a conjugated polymer, which is able to absorb the solar light as well as to conduct holes. Several kinds of inorganic

33

nanocrystals, CdSe, ZnO, CdS, and TiO_2 are reported as charge acceptors.[90–93] Also, various conjugated polymers are good candidates for BHJ solar cells, such as (2-methoxy, 5-(2-ethyl-hexy-loxy)-p-phenyl vinylene) (MEH-PPV), poly(3 -hexylthiophene) (P3HT), poly(alkyl-thiophenes) (PATs), poly[2-methoxy - 5 - (30, 70- dimethyloctyloxy)-p-phenylenevinylene] $(OC_1C_{10}$-PPV) and poly(2-methoxy-5-(3,7-dimethyloctyloxy)-1,4-phenylene- vinylene) (MDMO-PPV).[94–97]
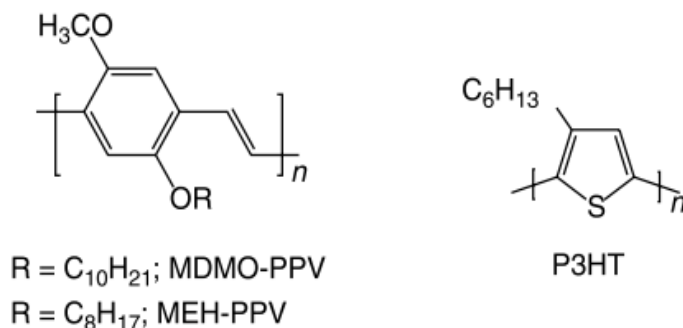
Figure 2.15. Chemical structures of conjugated polymers used as donors in BHJ solar cells

Conjugated polymers were first reported in 1958 by Hoegel et al. [98] who proposed its practical use as an electro-photographic agent. In the 1970s, it was discovered that certain conjugated polymers, notably poly(sulphur nitride) and polyacetylene could be made highly conductive in the presence of certain dopants. In 1982, Weinberger et al. [99] investigated the use of polyacetylene as the active material in an Al/polyacetylene/graphite cell. The cell had a low open-circuit voltage of only 0.3 V and a low QE of only 0.3%. Later, Glenis et al.[100] investigated different polythiophenes.

2.4.3.1. TiO₂ NPs and Conjugated Polymers-based BHJ solar cells

Nanostructured TiO_2 has been studied as a photovoltaic material since the 1980s, when the first observations of efficient photoinduced charge injection from dyes into TiO_2 were reported [101]. These studies established the basis for dye-sensitized solar cells[102]. The sensitization of TiO_2 by conjugated polymers or molecular films rather than by chemically adsorbed dye monolayer became of interest in the late 1990s following the first reports of photocurrent generation from conjugated polymer-based heterojunctions. Several studies

established that efficient photoinduced electron transfer from conjugated polymers into TiO_2 was possible [102–104]. Compared to dye-sensitized solar cells, the solid nanostructured TiO_2-polymer solar cell has the advantage of utilizing the complete heterostructure for exciton dissociation, potentially leading to thinner devices, since the entire polymer-filled pore volume is available for exciton generation rather than only a dye monolayer at the TiO_2 surface. Further, the rigid structure of TiO_2 offers better mechanical stability compared to the organic PVs.

Examples of blends from TiO_2 nanoparticles and conjugated polymers have shown only moderate external quantum efficiencies of a few percent and short circuit currents of tens of microamperes.[105–108] Devices efficiencies have been reported recently for blends of isotropic TiO_2 particles with P3HT ($\eta = 0.42\%$, AM 1, 100 mW/cm^2),[106] and elongated TiO_2 rods in MEH–PPV ($\eta = 0.49\%$, AM 1.5, 100 mW/cm^2).[107]

Despite promising EQE values, the power conversion efficiency values of devices have were low compared to those achieved using the same polymers in polymer–fullerene blends. The main factors limiting the performance include: incomplete distribution of the nanoparticles into the conjugated polymer matrix; sub-optimum nanostructure morphology where small quantity of the polymer volume lies within an exciton-diffusion length of the interface; poor charge transport in the metal oxide component itself; and a less than optimum photovoltage as a result of an unnecessarily large driving force for interfacial charge separation.

Fabricating TiO_2/polymer bulk heterojunction structures is an effective way to improve the excitation dissociation in hybrid PV cells. Petrella et al.[105,109] reported the photoinduced charge transfer and the recombination of MEH-PPV and TiO_2 nanorods (NRs) capped with oleic acid (OLA), but the power transfer efficiency was not given. Subsequently, Su et al.[107] reported a PCE of 0.49% for MEH-PPV/TiO_2 hybrid PV device by inserting a thin layer of TiO_2 NRs on the top of TiO_2/MEH-PPV hybrid layer. For further improve of the property of the hybrid polymer/TiO_2 NRs, it is very important to choose an appropriate ligand to exchange the OLA at the surface of TiO_2 NRs.
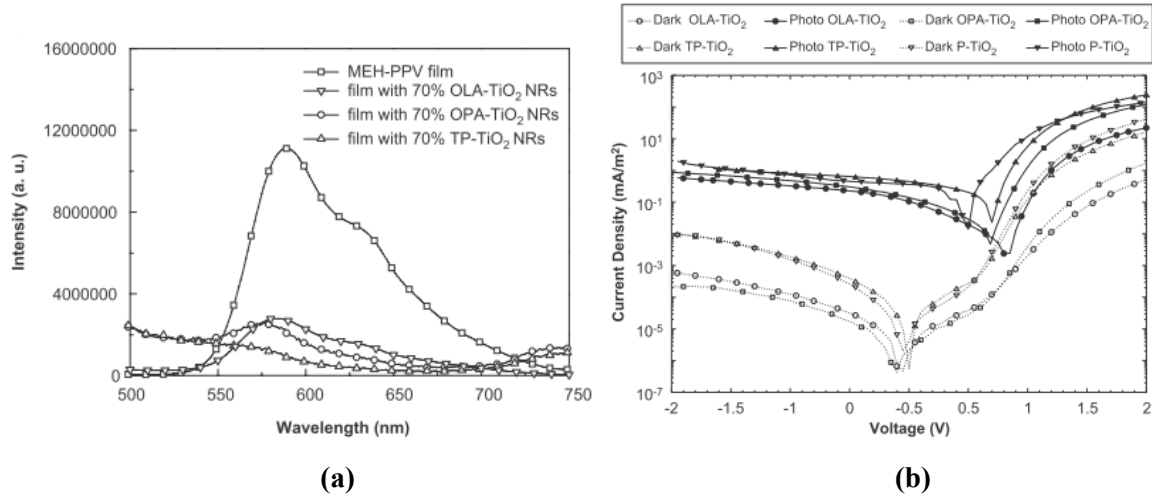
Figure 2.16. (a)The PL spectra from MEH-PPV: TiO$_2$ layers of 70% TiO$_2$ content with different capped ligands. (b) The J-V characteristics of the PV devices under AM 1.5 solar simulator (100 mW/cm^2).

While studying the PV properties of bulk heterojunction devices from MEH-PPV and TiO$_2$ NRs modified by different ligands (OLA, n-octyl-phosphonic (OPA), thiophenol (TP)) and TiO$_2$ with thoroughly cleaned surface, Liu et al.[108] reported that TiO$_2$ NRs modified with thiophenol (TP–TiO$_2$) showed best PV performance. They obtained a fill factor of around 0.34, an open-circuit voltage of approximately 0.70 V, and a power conversion efficiency of 0.16% at AM 1.5 solar simulator (100 mW/cm^2). Compared with the P-TiO$_2$, OPA- TiO$_2$ and OLA-TiO$_2$ NRs, the most effective exciton dissociation at MEH-PPV/TP–TiO$_2$ interface is due to the thiophenol capping, which is consistent with the PL quenching ability (Figure 2.16a).

Table 2.1. Photovoltaic properties of hybrid MEH-PPV/TiO$_2$ NRs capped by different ligands

TiO$_2$ NRs	Content of TiO$_2$ NRs	V$_{OC}$ (V)	I$_{SC}$ (mA cm^{-2})	FF (%)	PCE (%)
OLA-TiO$_2$ NRs	70	0.75	0.051	28	0.016
OPA-TiO$_2$ NRs	70	0.7	0.15	31	0.053
P-TiO$_2$ NRs	70	0.5	0.365	37	0.096
TP-TiO$_2$ NRs	70	0.7	0.456	34	0.157

Another strategy to improve the morphology of blend devices consists of using elongated nanocrystals, such as rods through synthetic control of the nanocrystal shape. The synthesis of TiO_2 NPs normally occurs using hydrothermal or sovolthermal process. Mixing these NPs into organic solvents generally leads to aggregate formation. For this reason, only 20–40 nm TiO_2 nanoparticles and conjugated polymers can be blended from common organic solvents. Petrella et al.[109] performed an extensive optical and photo-electrochemical study of blended systems composed of organic-capped TiO_2 crystals with a spherical (d ~ 5 nm) or rod-like (d ~ 3–4 nm, l = 25–30 nm) morphology and MEH-PPV. The blend exhibited higher photocurrents than those obtained with the single components, in agreement with the enhancement of MEH-PPV photo-excited electron transfer to TiO_2. In general, the use of spherical TiO_2 nanocrystals provided higher photo-electrochemical responses than their rod-like counterparts. The reported results also suggested that such MEH-PPV/TiO_2 heterojunctions may be exploited as potential active layers in photovoltaic and photo-electrochemical devices.
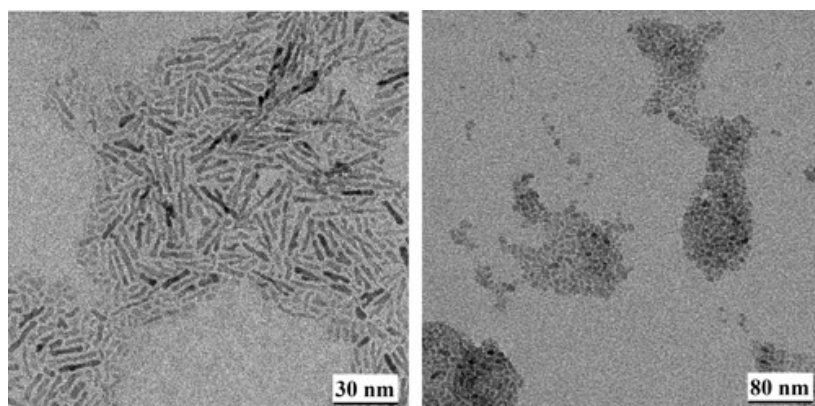
Figure 2.17. TEM of TiO_2 nanorods (a) and dots (b), obtained by hydrolysis method at 100°C: (a) OLEA 35 g, TTIP 5 mmol, 2M TMAO 5 ml; (b) OLEA 35 g, EG 3.2 g, TTIP 1 mmol, TMAO 4 mmol [109].

Kwong et al.[106] developed efficient solar cell devices by incorporating 60 wt% TiO_2 and a ~100 nm thick TiO_2:P3HT film spin coated from xylene. The obtained AM1 power conversion efficiency was 0.06% for pure P3HT, 0.01% for 20%-30% of TiO_2, 0.08% for 40% of TiO_2, 0.27% for 50% TiO_2, 0.42% for 60% TiO_2, and 0.07% for 70% TiO_2. For low

TiO$_2$ concentration, the cell performance is inferior to that of the pure P3HT, while for the TiO$_2$ concentration of 50% and 60%, considerable improvement in AM1 power conversion efficiency was obtained. However, for TiO$_2$ concentration of 70% and higher, a good quality uniform films could not be produced, so that the device performance worsened and the efficiency became comparable to that of pure P3HT (Figure 2.18a,b).
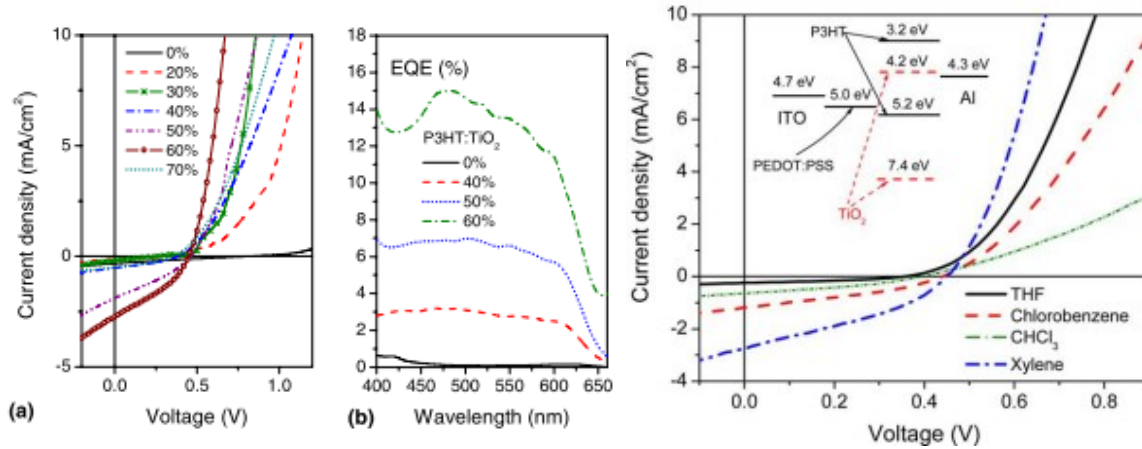
Figure 2.18. (a) J–V characteristics for P3HT:TiO$_2$ cells for different TiO$_2$ concentrations. (b) The comparison between external quantum efficiency (EQE) for nanocomposite and pure P3HT cells. (c) J–V characteristics of P3HT:TiO$_2$ cells with P3HT:TiO$_2$ films spin-coated from different solvents. Inset:g shows the energy diagram of the devices.

Figure 2.18c shows J–V characteristics for P3HT:TiO$_2$ cells with 60% of nanoparticle concentration prepared from different solvents. The obtained AM1 power conversion efficiencies are 0.03% for chloroform, 0.09% for THF, 0.17% for chlorobenzene, and 0.42% for xylene. As the solvent evaporation rates influence the surface morphology of polymer films [110], THF and chloroform have one order of magnitude higher vapor pressure compared to xylene, and hence evaporate significantly faster than xylene and chlorobenzene. In addition to solvent evaporation rate, the solvating power may significantly affect the morphology, since a good solvent could lead to a more extended polymer chain in solid state. Thus, a good solvent for P3HT with lower solvent evaporation rate may favor better mixing of the components, resulting in improved exciton dissociation and short circuit current density. The best and completed ITO/PEDOT:PSS/nc-TiO$_2$:P3HT/Al devices gave J_{SC}= 2.759 mA/cm^2, V_{OC} = 0.44 V, FF= 0.396, and PEC= 0.424% using xylene as solvent.

2.4.3.2. Modified-TiO₂ NPs and Conjugated Polymers-based BHJ solar cells

Several reports on various systems agree that the interface between the donor and the acceptor plays a crucial role for processes of charge separation and recombination. The commonly used solution processing for fully organic solar cells does not allow direct control of this interface. In contrast, metal oxide nanostructures can be easily modified in HSCs. Surface treatments, doping and the application of core-shell structures offer the potential to increase charge separation yield, reduce the recombination and enhance both V_{OC} and I_{SC}, resulting in more efficient PV devices.

Besides surface modifications, doping of metal oxides is a versatile method to influence charge transport properties and the location of valence and conduction bands. By doping ZnO with Mg, Olson et al. [111] were able to double the V_{OC} for ZnO-P3HT hybrid devices. An alloy of ZnMgO results in a reduced band offset and therefore allows an increased potential. For Mg contents up to 25%, they were able to decrease the effective work function from -4.2 eV to -3.9 eV resulting in an increase of V_{OC} from 0.5 V to more than 0.9 V. As mentioned above, similar effects have been reported for TiO₂ doped with Ta or N.[112,113] For N-doping, Vitiello et al.[114] were also able to show enhanced photoactivity of TiO₂ nanotubes in the visible range.

To simultaneously optimize both surfaces of the metal oxide and charge transport properties of the nanostructure, core-shell morphologies have been considered. Metal oxide nanostructures are coated with a thin layer of another material thus combining high mobility of the inner material with high charge selectivity of the coating.

Furthermore, nanometer-sized crystals of inorganic semiconductors are another interesting class of low-dimensional materials with useful optical and electronic properties. When the size of the nanocrystal is smaller than that of the exciton in the bulk semiconductor, quantum dot semiconductors (QDs), the lowest energy optical transition is significantly increased in energy due to quantum confinement. The absorbed and emitted energy can thus be tuned by changing the size of the nanocrystal. For example, by changing the size from 6 to 2 nm, the energy gap can be tuned from 2.6 to 3.1 eV in CdS and from 2.0 to 2.6 eV in CdSe; hence it makes them interesting optical materials of in solar cell application.[90,94,115–118]

At present, there are two main schemes for the deposition of NC sensitizers onto the surface of another NC, which include (i) introducing organic linker-molecules that bridge the colloids between two adjacent NCs, and (ii) growing NCs directly onto the oxide surface via chemical bath deposition (CBD) or successive ionic layer adsorption and reaction (SILAR) process[119]. For example, the former approach has been successfully employed to the following couples: CdS-TiO$_2$, CdSe-TiO$_2$, CdS-ZnO, CdTe-CdSe, and PbS-TiO$_2$.[120–125] The main drawback of this method is the presence of organic spacers between the nanocrystals and oxide domains, which increase the tunneling barrier between excited states of two semiconductors, causing a decrease in electron transfer probability. In addition, a number of experimental works have demonstrated that organic linkers can also serve as carrier traps, which further reduce the electron transfer rate.

Acharya et al.[125] demonstrated a facile method for developing PbS-sensitized TiO$_2$ films, which combines the benefits of the hot-injection colloidal route to the synthesis of monodisperse PbS NC sensitizers. The processes allowed a high-temperature growth of the PbS sensitizer directly onto the surface of TiO$_2$, where a controlled tuning of PbS domain sizes in the 2−20 nm range with an average dispersion of PbS diameters between 9 and 14% (Figure 2.19). Owing to a sequential two-step approach to the synthesis of TiO$_2$/PbS NCs, the size and the shape of TiO$_2$ domains can be well tuned, which provides an additional avenue for optimizing the transport of photoinduced carriers through an array of TiO$_2$/PbS NPs.
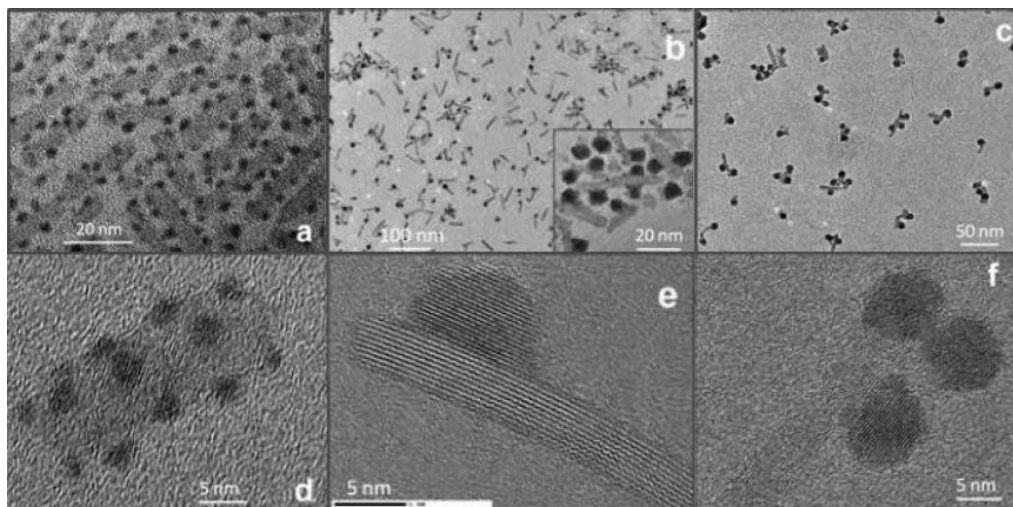
Figure 2.19. TEM of PbS/TiO₂ nanocomposites fabricated under different conditions (a) high concentration of OA results in the formation of small-diameter (d < 3 nm) PbS domains. (b) The formation of single, large-diameter PbS NCs (d > 4) when the concentration of OA in the solution is low. (c) The formation of multiple large-diameter PbS NCs per single nanorod occurs when the concentration of OA is low, and concentrations of Pb and S precursors are high. (d−f) HRTEM images of nanocomposites shown in (a−c), respectively.

The absorption profile in Figure 2.20b shows a small excitonic peak near 600 nm; its spectral position agrees well with the expected band gap absorption in 2.3 nm PbS NCs. This feature is absent in the spectrum of mixed PbS/TiO₂ heterostructures (green curve), possibly due to the overlapping absorption of large-diameter PbS NCs. Likewise, there is no clear indication of band edge transitions in PbS/TiO₂ NPs, comprising only large-diameter PbS NCs (d = 4.2 nm). The absence of the excitonic peak in the latter case cannot be attributed to the sample inhomogeneity alone because the size dispersion of PbS NCs in these heterostructures is only 12% and is likely to arise from excitations of intermediate states that exist at the interface of PbS and TiO₂ domains.
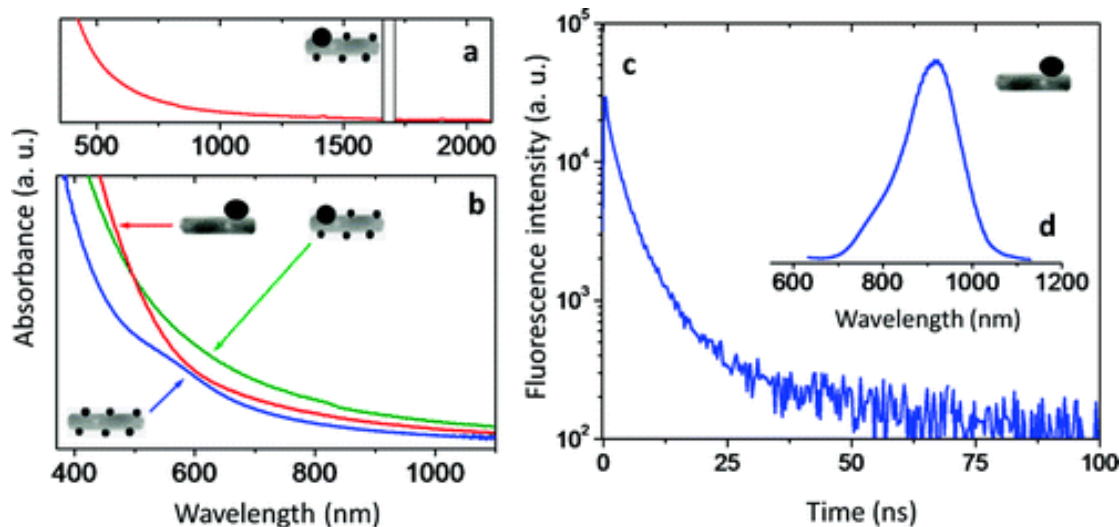
Figure 2.20. Optical properties of PbS/TiO₂. (a−b) Absorbance of PbS/TiO₂ nanocomposites representing several structural types. (c) Fluorescence intensity decay and (d) emission profile of PbS/TiO₂ heterostructures containing 4.2 nm PbS NCs.

PbS/TiO₂ heterostructures comprising small-diameter PbS NCs showed very weak or no fluorescence in the energy range corresponding to 1S(e)-1S(h) carrier recombination, whereas NPs containing larger PbS domains (d > 4) generally produced somewhat stronger emission in the near-infrared (λ = 800−1200 nm). This result is consistent with the prediction that small-diameter PbS are more likely to inject excited carriers into TiO₂, leaving only a small fraction of excited population to decay via radiative channels.

In their study on the effect of Te content in mixed semiconductor $CdSe_xTe_{1-x}$, Zhou et al.[124] synthesized a series of ternary tetrapodal nanocrystals of $CdSe_xTe_{1-x}$ with x = 0 (CdTe), 0.23, 0.53, 0.78, 1 (CdSe) and used them to fabricate hybrid nanocrystal/polymer solar cell devices. It was found that, under identical experimental conditions, V_{oc}, the J_{sc} and power conversion efficiency (η) of the devices increased with increasing Se content in the $CdSe_xTe_{1-x}$ nanocrystals. For convenience, $CdSe_{0.23}Te_{0.77}$, $CdSe_{0.53}Te_{0.47}$ and $CdSe_{0.78}Te_{0.22}$ are respectively denoted as Na1, Na2 and Na3 in the following Table 2.2 and Figure 2.21.

The photovoltaic properties of the hybrid $CdSe_xTe_{1-x}$ nanocrystals/MEH-PPV solar cells were systematically investigated with different compositions of the nanocrystals in ambient condition. The corresponding I–V curves are shown in Figure 2.21. From these

curves, the V_{oc}, J_{sc}, the FF, and η were calculated (see Table 2.2). The device based on CdTe without a Se component in the nanocrystals shows a relatively poor photovoltaic property with J_{sc} of 0.024 mA/cm^{-2}, V_{oc} of 0.33 V, and η of only 0.003%. When increasing the Se content in the nanocrystals, the performance of the devices improves steadily. After Te was totally substituted by Se, the efficiency increased to 1.13%, almost 400 times greater than that without Se component, and the J_{sc} and V_{oc} also significantly increased.
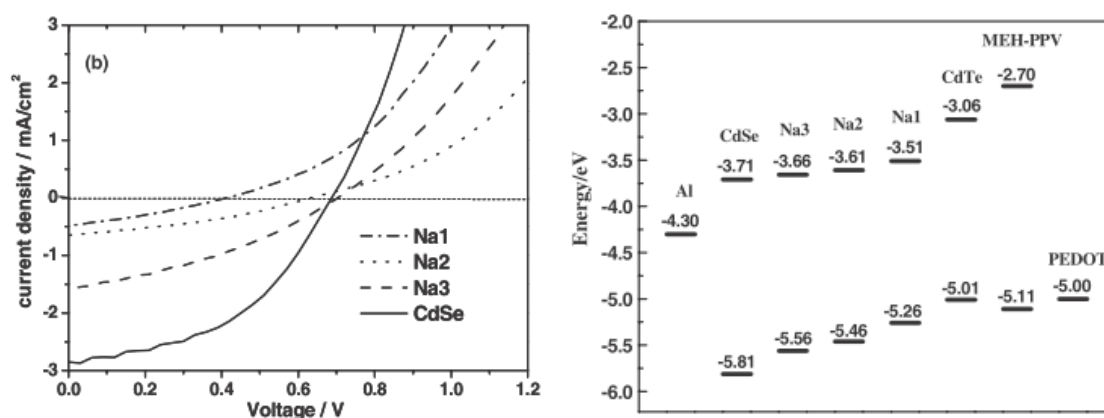
Figure 2.21. (LEFT) J–V curves of the BHJs based on MEH-PPV and the nanocrystals of Na1, Na2, Na3 and CdSe under illumination of AM1.5, 80 mW/cm^{-2}. (RIGHT) Band gap energy level positions of MEH-PPV and NC determined by CV measurements.

Table 2.2. Photovoltaic properties of BHJs based on MEH-PPV and various nanocrystals under the illumination of AM1.5, 80 mW/cm^{-2}

Nanocrystals in the hybrid solar cells	V_{OC} (V)	(J_{SC}) (mA cm^{-2})	FF	η (%)
CdTe	0.33	0.024	0.33	0.003
Na1	0.42	0.48	0.3	0.075
Na2	0.63	0.65	0.35	0.18
Na3	0.69	1.57	0.36	0.49
CdSe	0.69	2.86	0.46	1.13

Figure 2.21 (right) indicates that the highest occupied molecular orbital (HOMO) and lowest unoccupied molecular orbital (LUMO) level positions of ternary nanocrystals Na1, Na2 and Na3. When comparing the energy levels, all nanocrystal LUMO levels are

lower than those of the polymer's. However, only the CdTe HOMO level exceeds the polymer HOMO level, indicating that change separation is forbidden between the two components, and allowed for the other nanocrystals. Efficient charge separation requires optimal energy differences between electron donor (polymer) and acceptor (nanocrystal). Figure 2.21 (right) also shows that the energy gap between the nanocrystals and the polymer increased with Se content for both HOMO and LUMO levels, explaining why the photovoltaic properties of the devices improved with increasing the Se content in $CdSe_xTe_{1-x}$.

2.5. Reference

(1)   Fujishima, A.; Honda, K. *Nature* **1972**, *238*, 37–38.

(2)   (a) Fujishima, A.; Rao, T. N.; Tryk, D. A. *J. Photochem. Photobiol. C Photochem. Rev.* **2000**, *1*, 1–21. (b) Fujiwara, A.; Matsuoka, Y.; Suematsu, H.; Ogawa, N. *Carbon N. Y.* **2004**, *42*, 919–922. (c) Ishibashi, K.; Fujishima, A.; Watanabe, T.; Hashimoto, K. *J. Photochem. Photobiol. A Chem.* **2000**, *134*, 139–142. (d) Ohko, Y.; Ando, I.; Niwa, C.; Tatsuma, T.; Yamamura, T.; Nakashima, T.; Kubota, Y.; Fujishima, A. *Environ. Sci. Technol.* **2001**, *35*, 2365–2368. (e) Ishibashi, K.; Fujishima, A.; Watanabe, T.; Hashimoto, K. *Electrochem. commun.* **2000**, *2*, 207–210. (f) Nakata, K.; Sakai, M.; Ochiai, T.; Murakami, T.; Takagi, K.; Fujishima, A. *Langmuir* **2011**, *27*, 3275–3278. (g) Ishiguro, H.; Nakano, R.; Yao, Y.; Kajioka, J.; Fujishima, A.; Sunada, K.; Minoshima, M.; Hashimoto, K.; Kubota, Y. *Photochem. Photobiol. Sci.* **2011**, *10*, 1825–1829. (h) Liu, B.; Nakata, K.; Zhao, X.; Ochiai, T.; Murakami, T.; Fujishima, A. *J. Phys. Chem. C* **2011**, *115*, 16037–16042. (i) FUJISHIMA, A.; ZHANG, X.; TRYK, D. *Surf. Sci. Rep.* **2008**, *63*, 515–582. (j) Nakata, K.; Udagawa, K.; Ochiai, T.; Sakai, H.; Murakami, T.; Abe, M.; Fujishima, A. *Mater. Chem. Phys.* **2011**, *126*, 484–487. (k) Zhao, T.; Liu, Z.; Nakata, K.; Nishimoto, S.; Murakami, T.; Zhao, Y.; Jiang, L.; Fujishima, A. *J. Mater. Chem.* **2010**, *20*, 5095.

(3)   Bach, U.; Lupo, D.; Comte, P.; Moser, J. E.; Weissortel, F.; Salbeck, J.; Spreitzer, H.; Gratzel, M. *Nature* **1998**, *395*, 583–585.

(4)   Kuang, D.; Brillet, J.; Chen, P.; Takata, M.; Uchida, S.; Miura, H.; Sumioka, K.; Zakeeruddin, S. M.; Grätzel, M. *ACS Nano* **2008**, *2*, 1113–1116.

(5)   Wang, H.; Oey, C. C.; Djurišić, A. B.; Man, K. K. Y.; Chan, W. K.; Xie, M. H.; Leung, Y. H.; Pandey, A.; Nunzi, J.; Lavoisier, B.; Cedex, A. *Proc. 2005 5th IEEE Conf. Nanotechnol.* **2005**, 1–4.

(6)   Wu, G.; Wang, J.; Thomas, D. F.; Chen, A. *Langmuir* **2008**, *24*, 3503–3509.

(7)   Holland, B. T. *Science (80-.).* **1998**, *281*, 538–540.

(8)   Landau, O.; Rothschild, A. *Sensors Actuators B Chem.* **2012**, *171-172*, 118–126.

(9)   Pfaff, G.; Reynders, P. *Chem. Rev.* **1999**, *99*, 1963–1982.

(10)   Águia, C.; Ângelo, J.; Madeira, L. M.; Mendes, A. *Polym. Degrad. Stab.* **2011**, *96*, 898–906.

(11)   Marchand, R.; Brohan, L.; Tournoux, M. *Mater. Res. Bull.* **1980**, *15*, 1129–1133.

(12)   Simons, P. Y.; Dachille, F. *Acta Crystallogr.* **1967**, *23*, 334–336.

(13)   Latroche, M.; Brohan, L.; Marchand, R.; Tournoux, M. *J. Solid State Chem.* **1989**, *81*, 78–82.

(14)   Sato, H.; Endo, S.; Sugiyama, M.; Kikegawa, T.; Shimomura, O.; Kusaba, K. *Science* **1991**, *251*, 786–788.

(15)   Nishio-Hamane, D.; Shimizu, A.; Nakahira, R.; Niwa, K.; Sano-Furukawa, A.; Okada, T.; Yagi, T.; Kikegawa, T. *Phys. Chem. Miner.* **2009**, *37*, 129–136.

(16)   Mo, S.; Ching, W. *Phys. Rev. B* **1995**, *51*, 13023–13032.

(17)   Tanaka, K.; Capule, M. F. V.; Hisanaga, T. *Chem. Phys. Lett.* **1991**, *187*, 73–76.

(18)   Leary, R.; Westwood, A. *Carbon N. Y.* **2011**, *49*, 741–772.

(19)   Diebold, U. *Surf. Sci. Rep.* **2003**, *48*, 53–229.

(20)   Wiggins, M. D.; Nelson, M. C.; Atta, C. R. *MRS Proc.* **2011**, *398*, 381.

(21)   Sclafani, A.; Palmisano, L.; Schiavello, M. *J. Phys. Chem.* **1990**, *94*, 829–832.

(22)   Carp, O.; Huismanb, C. L.; Rellerb, A. *Prog. Solid State Chem.* **2004**, *32*, 33–177.

(23)   Reidy, D. J.; Holmes, J. D.; Morris, M. a. *Ceram. Int.* **2006**, *32*, 235–239.

(24)   Srinivasan, S. S.; Wade, J.; Stefanakos, E. K. *J. Nanomater.* **2006**, *2006*, 1–7.

(25)   Wang, B.; Kerr, L. L. *J. Solid State Electrochem.* **2011**, *16*, 1091–1097.

(26)   Li, Y.; Xie, W.; Hu, X.; Shen, G.; Zhou, X.; Xiang, Y.; Zhao, X.; Fang, P. *Langmuir* **2010**, *26*, 591–597.

(27) Li, Y.; Lu, P.; Jiang, M.; Dhakal, R.; Thapaliya, P.; Peng, Z.; Jha, B.; Yan, X. *J. Phys. Chem. C* **2012**, *116*, 25248–25256.

(28) Cowan, A. J.; Barnett, C. J.; Pendlebury, S. R.; Barroso, M.; Sivula, K.; Grätzel, M.; Durrant, J. R.; Klug, D. R. *J. Am. Chem. Soc.* **2011**, *133*, 10134–10140.

(29) Ren, Y.; Chen, M.; Zhang, Y.; Wu, L. *Langmuir* **2010**, *26*, 11391–11396.

(30) Vinodgopal, K.; Bedja, I.; Kamat, P. V. *Chem. Mater.* **1996**, *8*, 2180–2187.

(31) Song, K. Y.; Park, M. K.; Kwon, Y. T.; Lee, H. W.; Chung, W. J.; Lee, W. I. *Chem. Mater.* **2001**, *13*, 2349–2355.

(32) Bessekhouad, Y.; Robert, D.; Weber, J. . *J. Photochem. Photobiol. A Chem.* **2004**, *163*, 569–580.

(33) De, G. .; Roy, A. M.; Bhattacharya, S. S. *Int. J. Hydrogen Energy* **1995**, *20*, 127–131.

(34) Li, W.; Li, D.; Chen, Z.; Huang, H.; Sun, M.; He, Y.; Fu, X. *J. Phys. Chem. C* **2008**, *112*, 14943–14947.

(35) Steinfeld, A. *Int. J. Hydrogen Energy* **2002**, *27*, 611–619.

(36) Kudo, A.; Omori, K.; Kato, H. *J. Am. Chem. Soc.* **1999**, *121*, 11459–11467.

(37) Zou, Z.; Arakawa, H. *J. Photochem. Photobiol. A Chem.* **2003**, *158*, 145–162.

(38) Kudo, A.; Miseki, Y. *Chem. Soc. Rev.* **2009**, *38*, 253–278.

(39) Williams, R. *J. Chem. Phys.* **1960**, *32*, 1505.

(40) Ellis, A. B.; Kaiser, S. W.; Bolts, J. M.; Wrighton, M. S. *J. Am. Chem. Soc.* **1977**, *99*, 2839–2848.

(41) St. John, M. R.; Furgala, A. J.; Sammells, A. F. *J. Phys. Chem.* **1983**, *87*, 801–805.

(42) Bamwenda, G. R.; Tsubota, S.; Nakamura, T.; Haruta, M. *J. Photochem. Photobiol. A Chem.* **1995**, *89*, 177–189.

(43) Sakthivel, S.; Shankar, M. V; Palanichamy, M.; Arabindoo, B.; Bahnemann, D. W.; Murugesan, V. *Water Res.* **2004**, *38*, 3001–3008.

(44) Wu, N.-L.; Lee, M.-S. *Int. J. Hydrogen Energy* **2004**, *29*, 1601–1605.

(45) Alenzi, N.; Liao, W.-S.; Cremer, P. S.; Sanchez-Torres, V.; Wood, T. K.; Ehlig-Economides, C.; Cheng, Z. *Int. J. Hydrogen Energy* **2010**, *35*, 11768–11775.

(46) Paunović, P.; Gogovska, D. S.; Popovski, O.; Stoyanova, A.; Slavcheva, E.; Lefterova, E.; Iliev, P.; Dimitrov, A. T.; Jordanov, S. H. *Int. J. Hydrogen Energy* **2011**, *36*, 9405–9414.

(47) Anpo, M. *J. Catal.* **2003**, *216*, 505–516.

(48) Subramanian, V.; Wolf, E.; Kamat, P. V. *J. Phys. Chem. B* **2001**, *105*, 11439–11446.

(49) Jakob, M.; Levanon, H.; Kamat, P. V. *Nano Lett.* **2003**, *3*, 353–358.

(50) Sayama, K.; Arakawa, H. *J. Chem. Soc. Faraday Trans.* **1997**, *93*, 1647–1654.

(51) Dholam, R.; Patel, N.; Adami, M.; Miotello, A. *Int. J. Hydrogen Energy* **2009**, *34*, 5337–5346.

(52) Ikeda, S.; Sugiyama, N.; Pal, B.; Marcí, G.; Palmisano, L.; Noguchi, H.; Uosaki, K.; Ohtani, B. *Phys. Chem. Chem. Phys.* **2001**, *3*, 267–273.

(53) Peng, S.; Li, Y.; Jiang, F.; Lu, G.; Li, S. *Chem. Phys. Lett.* **2004**, *398*, 235–239.

(54) Sun, T.; Fan, J.; Liu, E.; Liu, L.; Wang, Y.; Dai, H.; Yang, Y.; Hou, W.; Hu, X.; Jiang, Z. *Powder Technol.* **2012**, *228*, 210–218.

(55) Szabo-Bardos, E.; Czili, H.; Horvath, A. *J. Photochem. Photobiol. A Chem.* **2003**, *154*, 195–201.

(56) Niishiro, R.; Kato, H.; Kudo, A. *Phys. Chem. Chem. Phys.* **2005**, *7*, 2241.

(57) Asahi, R.; Morikawa, T.; Ohwaki, T.; Aoki, K.; Taga, Y. *Science* **2001**, *293*, 269–271.

(58) Wang, C.; Hu, Q.; Huang, J.; Wu, L.; Deng, Z.; Liu, Z.; Liu, Y.; Cao, Y. *Appl. Surf. Sci.* **2013**, *283*, 188–192.

(59) Wang, C.; Hu, Q.-Q.; Huang, J.-Q.; Deng, Z.-H.; Shi, H.-L.; Wu, L.; Liu, Z.-G.; Cao, Y.-G. *Int. J. Hydrogen Energy* **2014**, *39*, 1967–1971.

(60) Krengvirat, W.; Sreekantan, S.; Mohd Noor, A.-F.; Negishi, N.; Oh, S. Y.; Kawamura, G.; Muto, H.; Matsuda, A. *Int. J. Hydrogen Energy* **2012**, *37*, 10046–10056.

(61) Dhanalakshmi, K. *Int. J. Hydrogen Energy* **2001**, *26*, 669–674.

(62) Sasikala, R.; Shirole, A.; Sudarsan, V.; Sakuntala, T.; Sudakar, C.; Naik, R.; Bharadwaj, S. R. *Int. J. Hydrogen Energy* **2009**, *34*, 3621–3630.

(63) So, W. *Int. J. Hydrogen Energy* **2004**, *29*, 229–234.

(64) Li, C.; Yuan, J.; Han, B.; Jiang, L.; Shangguan, W. *Int. J. Hydrogen Energy* **2010**, *35*, 7073–7079.

(65) Wu, G.; Tian, M.; Chen, A. *J. Photochem. Photobiol. A Chem.* **2012**, *233*, 65–71.

(66) Jang, J. S.; Ji, S. M.; Bae, S. W.; Son, H. C.; Lee, J. S. *J. Photochem. Photobiol. A Chem.* **2007**, *188*, 112–119.

(67) Bard, A. J. *J. Photochem.* **1979**, *10*, 59–75.

(68) Sasaki, Y.; Iwase, a; Kato, H.; Kudo, a. *J. Catal.* **2008**, *259*, 133–137.

(69) Moon, S.; Mametsuka, H.; Tabata, S.; Suzuki, E. *Catal. Today* **2000**, *58*, 125–132.

(70) Abe, R.; Sayama, K.; Arakawa, H. *Chem. Phys. Lett.* **2003**, *371*, 360–364.

(71) Nada, A. A.; Barakatb, M. H.; Hameda, H. A.; Mohameda, N. R.; Verizogluc, T. N. *Int. J. Hydrogen Energy* **2005**, *30*, 687–691.

(72) Abe, R.; Sayama, K.; Domen, K.; Arakawa, H. *Chem. Phys. Lett.* **2001**, *344*, 339–344.

(73) Galinska, A.; Walendziewski, J. *Energy & Fuels* **2005**, *19*, 1143–1147.

(74) Li, Y.; Lu, G.; Li, S. *Chemosphere* **2003**, *52*, 843–850.

(75) Becquerel, A. E. *Comptes Rendus L'Academie des Sci.* **1839**, *9*, 561– 567.

(76) Chapin, D. M.; Fuller, C. S.; Pearson, G. L. *J. Appl. Phys.* **1954**, *25*, 676.

(77) Liu, J.; Tanaka, T.; Sivula, K.; Alivisatos, a P.; Fréchet, J. M. J. *J. Am. Chem. Soc.* **2004**, *126*, 6550–6551.

(78) Wallace, G. G.; Chen, J.; Mozer, A. J.; Forsyth, M.; Macfarlane, D. R.; Wang, C. *Mater. Today* **2009**, *12*, 20–27.

(79) Ginger, D. S.; Greenham, N. C. *Synth. Met.* **2001**, *124*, 117–120.

(80) Salafsky, J. *Phys. Rev. B* **1999**, *59*, 10885–10894.

(81) Nelson, J. *Curr. Opin. Solid State Mater. Sci.* **2002**, *6*, 87–95.

(82) Markvart, T.; Castaner, L. *Practical Handbook of Photovoltaics: Fundamentals and Applications*; 1st ed.; Elsevier Science Ltd, 2003; p. 512.

(83) Brabec, C. J.; Sariciftci, N. S.; Hummelen, J. C. *Adv. Funct. Mater.* **2001**, *11*, 15–26.

(84) Mihailetchi, V. D.; Koster, L. J. a.; Blom, P. W. M. *Appl. Phys. Lett.* **2004**, *85*, 970.

(85) Kim, Y.; Choulis, S. a.; Nelson, J.; Bradley, D. D. C.; Cook, S.; Durrant, J. R. *Appl. Phys. Lett.* **2005**, *86*, 063502.

(86) Padinger, F.; Rittberger, R. S.; Sariciftci, N. S. *Adv. Funct. Mater.* **2003**, *13*, 85–88.

(87) Reyes-Reyes, M.; Kim, K.; Dewald, J.; López-Sandoval, R.; Avadhanula, A.; Curran, S.; Carroll, D. L. *Org. Lett.* **2005**, *7*, 5749–5752.

(88) Li, G.; Shrotriya, V.; Huang, J.; Yao, Y.; Moriarty, T.; Emery, K.; Yang, Y. *Nat. Mater.* **2005**, *4*, 864–868.

(89) Ma, W.; Yang, C.; Gong, X.; Lee, K.; Heeger, A. J. *Adv. Funct. Mater.* **2005**, *15*, 1617–1622.

(90) Verma, D.; Ranga Rao, A.; Dutta, V. *Sol. Energy Mater. Sol. Cells* **2009**, *93*, 1482–1487.

(91) Huynh, W. U.; Dittmer, J. J.; Alivisatos, a P. *Science* **2002**, *295*, 2425–2427.

(92) Wang, L.; Liu, Y.; Jiang, X.; Qin, D.; Cao, Y. *J. Phys. Chem. C* **2007**, *111*, 9538–9542.

(93) Roberson, L. B.; Poggi, M. A.; Kowalik, J.; Smestad, G. P.; Bottomley, L. A.; Tolbert, L. M. *Coord. Chem. Rev.* **2004**, *248*, 1491–1499.

(94) Kang, Y.; Kim, D. *Sol. Energy Mater. Sol. Cells* **2006**, *90*, 166–174.

(95) Ram, M. K.; Sarkar, N.; Bertoncello, P.; Sarkar, A.; Narizzano, R.; Nicolini, C. *Synth. Met.* **2001**, *122*, 369–378.

(96) Wu, M.-C.; Lo, H.-H.; Liao, H.-C.; Chen, S.; Lin, Y.-Y.; Yen, W.-C.; Zeng, T.-W.; Chen, Y.-F.; Chen, C.-W.; Su, W.-F. *Sol. Energy Mater. Sol. Cells* **2009**, *93*, 869–873.

(97) Al-Ibrahim, M. *Sol. Energy Mater. Sol. Cells* **2004**, *85*, 13–20.

(98) Heeger, A. J. *J. Phys. Chem. B* **2001**, *105*, 8475–8491.

(99) Weinberger, B. R.; Akhtar, M.; Gau, S. C. *Synth. Met.* **1982**, *4*, 187–197.

(100) Glenis, S.; Tourillon, G.; Garnier, F. *Thin Solid Films* **1986**, *139*, 221–231.

(101) Vlachopoulos, N.; Liska, P.; Augustynski, J.; Graetzel, M. *J. Am. Chem. Soc.* **1988**, *110*, 1216–1220.

(102) O'Regan, B.; Grätzel, M. *Nature* **1991**, *353*, 737–740.

(103) Van Hal, P. A.; Christiaans, M. P. T.; Wienk, M. M.; Kroon, J. M.; Janssen, R. A. J. *J. Phys. Chem. B* **1999**, *103*, 4352–4359.

(104) Arango, A. C.; Carter, S. a.; Brock, P. J. *Appl. Phys. Lett.* **1999**, *74*, 1698.

(105) Petrella, A.; Tamborra, M.; Cozzoli, P. .; Curri, M. .; Striccoli, M.; Cosma, P.; Farinola, G. .; Babudri, F.; Naso, F.; Agostiano, A. *Thin Solid Films* **2004**, *451-452*, 64–68.

(106) Kwong, C. Y.; Djurišić, A. B.; Chui, P. C.; Cheng, K. W.; Chan, W. K. *Chem. Phys. Lett.* **2004**, *384*, 372–375.

(107) Zeng, T.; Lin, Y.; Lo, H. *Nanotechnology* **2006**, *17*, 5387–5392.

(108) Liu, J.; Wang, W.; Yu, H.; Wu, Z.; Peng, J.; Cao, Y. *Sol. Energy Mater. Sol. Cells* **2008**, *92*, 1403–1409.

(109) Petrella, A.; Tamborra, M.; Curri, M. L.; Cosma, P.; Striccoli, M.; Cozzoli, P. D.; Agostiano, A. *J. Phys. Chem. B* **2005**, *109*, 1554–1562.

(110) Strawhecker, K. E.; Kumar, S. K.; Douglas, J. F.; Karim, A. *Macromolecules* **2001**, *34*, 4669–4672.

(111) Olson, D. C.; Shaheen, S. E.; White, M. S.; Mitchell, W. J.; van Hest, M. F. A. M.; Collins, R. T.; Ginley, D. S. *Adv. Funct. Mater.* **2007**, *17*, 264–269.

(112) Feng, X.; Shankar, K.; Paulose, M.; Grimes, C. a. *Angew. Chem. Int. Ed. Engl.* **2009**, *48*, 8095–8098.

(113) Yu, H.; Zhang, Z.; Han, M.; Hao, X.; Zhu, F. *J. Am. Chem. Soc.* **2005**, *127*, 2378–2379.

(114) Sun, Y.; Fuge, G. M.; Fox, N. a.; Riley, D. J.; Ashfold, M. N. R. *Adv. Mater.* **2005**, *17*, 2477–2481.

(115) Vossmeyer, T.; Katsikas, L.; Giersig, M.; Popovic, I. G.; Diesner, K.; Chemseddine, A.; Eychmueller, A.; Weller, H. *J. Phys. Chem.* **1994**, *98*, 7665–7673.

(116) Li, L.; Hu, J.; Yang, W.; Alivisatos, A. P. *Nano* **2001**, 0–2.

(117) Greenham, N.; Peng, X.; Alivisatos, A. *Phys. Rev. B* **1996**, *54*, 17628–17637.

(118) Zhou, Y.; Riehle, F. S.; Yuan, Y.; Schleiermacher, H.; Niggemann, M.; Urban, G. a.; Krüger, M. *Appl. Phys. Lett.* **2010**, *96*, 013304.

(119) Pathan, H. M.; Lokhande, C. D. *Bull. Mater. Sci.* **2004**, *27*, 85–111.

(120) Fujii, H.; Inata, K.; Ohtaki, M.; Eguchi, K.; Arai, H. *J. Mater. Sci.* **2001**, *6*, 527–532.

(121) Peter, L. M.; Riley, D. J.; Tull, E. J.; Wijayantha, K. G. U. *Chem. Commun.* **2002**, 1030–1031.

(122) Mora-Sero, I.; Bisquert, J.; Dittrich, T.; Belaidi, A.; Susha, A. S.; Rogach, A. L. *J. Phys. Chem. C* **2007**, *111*, 14889–14892.

(123) Kongkanand, A.; Tvrdy, K.; Takechi, K.; Kuno, M.; Kamat, P. V. *J. Am. Chem. Soc.* **2008**, *130*, 4007–4015.

(124) Zhou, Y.; Li, Y.; Zhong, H.; Hou, J.; Ding, Y.; Yang, C.; Li, Y. *Nanotechnology* **2006**, *17*, 4041–4047.

(125) Acharya, K. P.; Hewa-Kasakarage, N. N.; Alabi, T. R.; Nemitz, I.; Khon, E.; Ullrich, B.; Anzenbacher, P.; Zamkov, M. *J. Phys. Chem. C* **2010**, *114*, 12496–12504.